1-1-2013

Structured Materials for Catalytic and Sensing Applications

Selma Hokenek
University of South Florida, shokenek@mail.usf.edu

Structured Materials for Catalytic and Sensing Applications

by

Selma Hokenek

A dissertation submitted in partial fulfillment
of the requirements for the degree of
Doctor of Philosophy
Department of Chemical and Biomedical Engineering
College of Engineering
University of South Florida

Major Professor: John N. Kuhn, Ph.D.
Scott W. Campbell, Ph.D.
Jeffrey A. Cunningham, Ph.D.
W. Garrett Matthews, Ph.D.
Venkat R. Bhethanabotla, Ph.D.

Date of Approval:
March 27, 2013

Keywords: nanoparticle shape control, nanoparticle size control, bimetallic, nickel, palladium, silver

Dedication

I would like to dedicate this work to my advisor, Dr. John Kuhn, without whom none of this would have been remotely possible, to my wonderful supportive family and friends, who have helped keep me focused through all the stressful moments, to my co-workers, who helped me out when I hit a roadblock or supplied ice cream when the occasion demanded, and to those students who take up the thread of this research after me, may their roads be smooth.

Acknowledgments

Funding for this work, provided by NREL subcontract No.8 XGB-0-40646-01, Hinkley Center for Solid and Hazardous Waste Management, a Florida Energy Systems Consortium Seed Grant, and the USF Internal Awards Program under Grant No. 0074332, are gratefully acknowledged. Portions of this work were performed at the DuPont-Northwestern-Dow Collaborative Access Team (DND-CAT) located at Sector 5 of the Advanced Photon Source (APS). DND-CAT is supported by E.I. DuPont de Nemours & Co., The Dow Chemical Company and the State of Illinois. Use of the APS was supported by the U.S. Department of Energy, Office of Science, Office of Basic Energy Sciences, under contract number DEAC02-06CH11357. Assistance from the DND-CAT beamline scientists, especially to Qing Ma, is greatly appreciated. For their assistance in nanoparticle synthesis, we would like to acknowledge undergraduates John Ammerman, Crystal Bennett, and Curtis Thompson. Additionally, we would like to thank Mr. Edward Haller for providing access to and troubleshooting for TEM imaging and Mr. Jay Bieber for his valuable advice and technical know-how. We would like to acknowledge the USF Nanotechnology Research and Education Center for providing access to and support for XRD, high resolution TEM, and STEM-EDX.

And last, but certainly not least, the wonderful Ms. Catherine Burton and the rest of the thesis format team who helped make writing this document as painless as possible.

Table of Contents

List of Tables iii

List of Figures iv

Abstract vii

Chapter 1: Introduction 1
1.1. Motivation and Objectives 1
1.1.1. Objectives 4
1.1.2. Hypotheses 5
1.2. Background and Significance 6
1.2.1. Polyol Synthesis 6
1.2.2. Active Site Correlation with Surface Planes 10
1.2.3. Surface Plasmon Resonance (SPR) 11
1.2.4. Ni-Pd Size and Shape Effects 11
1.2.5. Ni-Pd Segregation 13
1.2.6. Ag-Pd Nanoparticles 14
1.2.7. Ni-Pd Composition Effects 17

Chapter 2: Analysis Techniques 19
2.1. Transmission Electron Microscopy (TEM) 19
2.2. X-Ray Diffraction (XRD) 20
2.3. Energy Dispersive X-ray Spectroscopy (EDS or EDX) 21
2.4. Ultraviolet-Visible Spectrometry (UV-VIS) 21
2.5. Mass Spectrometry (MS) 22
2.5.1. Temperature Programmed Reduction (TPR) 22
2.5.2. Temperature Programmed Reaction Spectroscopy (TPRS) 23
2.5.3. Temperature Programmed Oxidation (TPO) 23
2.6. X-Ray Absorption Spectroscopy (XAS) 23

Chapter 3: Role of Pd Nanoparticle Size in Methanol Decomposition Reaction 25
3.1. Experimental Details 25
3.1.1. Polyol Synthesis 25
3.1.2. Silica Support 26
3.2. Characterisation Techniques 27
3.3. Results and Discussion 30
3.4. Conclusions 38

Chapter 4: Synthesis and Characterization of Shape-Controlled Ni-Pd Nanoparticles 40
4.1. Experimental Details 40
4.2. Characterisation Techniques 41
4.3. Results and Discussion 42
4.4. Conclusions 49

Chapter 5: Effect of Shape and Composition on SPR in Ag and Pd Nanoparticles 51
5.1. Experimental Details 52
5.2. Characterisation Techniques 54
5.3. Results and Discussion 55
5.4. Conclusions 66

Chapter 6: Conclusions and Outlook 68

References 71

Appendices 85
Appendix 1: EXAFS Experimental Details 86
Appendix 2: Casino Monte Carlo Simulations 87
Appendix 3: Journal Reprint Permissions 90

About the Author .... End Page

List of Tables

Table 1: Molar Ratios and Calculated mg Amounts of Pd(II) and Pd(IV) Precursors 26

Table 2: Change in Coking Rate with Particle Size 38

Table 3: Bimetallic NiPd Nanocube Synthesis Characteristics 42

Table 4: Ag Nanoparticle Shape Distributions. 55

List of Figures

Figure 1: Schematic representation of a polyol synthesis for the production of Ag nanoparticles. 6

Figure 2: Surface planes of differently shaped nanoparticles 7

Figure 3: Generalised representation of the La Mer model of nucleation 8

Figure 4: Effect of synthesis conditions on surface facet growth rate 9

Figure 5: Principles of XAS. 24

Figure 6: Schematic representation of the one-pot polyol synthesis method for fabricating monometallic Pd nanoparticles of controlled sizes 27

Figure 7: XRD spectra of Pd nanoparticles synthesized through the one-pot polyol synthesis 31

Figure 8: Average diameter measured in TEM and calculated Scherrer diameter of synthesized Pd nanoparticles 32

Figure 9: XANES region as a function of percentage of Pd particle size 33

Figure 10: Hydrogen production during methanol dry reforming as a function of reaction temperature, and (inset) peak methanol conversion TOF versus particle size calculated in terms of mol sec-1 atom-1 35

Figure 11: TPRS results for the methanol decomposition reaction run on the smallest (0% Pd(IV)) Pd catalysts. 36

Figure 12: Reaction network as determined through TPRS studies 37

Figure 13: (left) HRTEM of a nanocube synthesized at a reduction temperature of 160°C, with a TTAB molar ratio of 30:1 43

Figure 14: Influence of molar ratio of bromide ion to metal atom on shape distribution in NiPd alloy nanoparticles (A: 15:1, B: 30:1, and C: 50:1) at a reduction temperature of 160°C 44

Figure 15: Influence of reduction temperature on shape distribution in NiPd alloy nanoparticles (A: 140°C, B: 160°C, and C: 180°C) with a TTAB:precursor molar ratio of 30:1 44

Figure 16: (left) The bright field STEM image of particles in the sample with the most cubes 45

Figure 17: (left) The bright field STEM image of particles in the sample with the most cubes and rods 46

Figure 18: XRD profiles of all NiPd nanoparticle samples 48

Figure 19: TEM images of Ag nanocubes and polyhedra taken at an acceleration voltage of 60 kV and a magnification of (A,C) 44kx, and (B,D) 180kx. 56

Figure 20: TEM images of Pd nanoboxes with (A) 10 nm Pd shell, (B) 6 nm Pd shell, and (C) 5 nm Pd shell 57

Figure 21: X-ray diffractograms of (A)Ag nanocubes, (E)Ag polyhedra, and Pd nanoboxes with (B)10 nm, (C) 6 nm, and (D) 5 nm wall thicknesses. 58

Figure 22: Deconvolution of Ag(111) and AgO(111) XRD peaks observed in Ag nanocubes. 59

Figure 23: SEM image of Ag nanocubes synthesized. 61

Figure 24: SEM image of an Ag nanocube and its corresponding EDS line scan 62

Figure 25: UV-Vis spectra of Ag nanocubes, polyhedra, and hollow Pd nanocubes. 63

Figure 26: UV-Vis spectra of physical mixtures of Ag polyhedra and as-synthesized Pd nanoboxes 63

Figure 27: Variation in UV-Vis peak positions of physical mixtures of Ag polyhedra and fractionated Pd nanoboxes 64

Figure 28: Variation in UV-Vis peak positions of physical mixtures of Ag cubes and fractionated 6 nm wall Pd nanoboxes 65

Figure A2-1: Simulated Ag nanocube under a 25 kV electron beam with 5 nm diameter..... 87

Figure A2-2: Simulated Ag nanocube under a 10 kV electron beam with 5 nm diameter..... 88

Figure A2-3: Simulated Ag nanocube under a 5 kV electron beam with 5 nm diameter..... 89

Abstract

The optical and chemical properties of the materials used in catalytic and sensing applications directly determine the characteristics of the resultant catalyst or sensor. It is well known that a catalyst needs to have high activity, selectivity, and stability to be viable in an industrial setting. The hydrogenation activity of palladium catalysts is known to be excellent, but the industrial applications are limited by the cost of obtaining catalyst in amounts large enough to make their use economical. As a result, alloying palladium with a cheaper, more widely available metal while maintaining the high catalytic activity seen in monometallic catalysts is, therefore, an attractive option. Similarly, the optical properties of nanoscale materials used for sensing must be attuned to their application. By adjusting the shape and composition of nanoparticles used in such applications, very fine changes can be made to the frequency of light that they absorb most efficiently.

The design, synthesis, and characterization of (i) size controlled monometallic palladium nanoparticles for catalytic applications, (ii) nickel-palladium bimetallic nanoparticles and (iii) silver-palladium nanoparticles with applications in drug detection and biosensing through surface plasmon resonance, respectively, will be discussed. The composition, size, and shape of the nanoparticles formed were controlled through the use of wet chemistry techniques. After synthesis, the nanoparticles were analyzed using physical and chemical characterization techniques such as X-Ray Diffraction (XRD), Transmission Electron Microscopy (TEM), and Scanning Transmission Electron

Microscopy- Energy-Dispersive Spectrometry (STEM-EDX). The Pd and Ni-Pd nanoparticles were then supported on silica for catalytic testing using mass spectrometry. The optical properties of the Ag-Pd nanoparticles in suspension were further investigated using ultraviolet-visible spectrometry (UV-Vis).

Monometallic palladium particles have been synthesized and characterized to establish the effects of nanoparticle size on catalytic activity in methanol decomposition. The physicochemical properties of the synthesized palladium-nickel nanoparticles will be discussed, as a function of the synthesis parameters. The optical characteristics of the Ag and Pd nanoparticles will be determined, with a view toward tuning the response of the nanoparticles for incorporation in sensors. Analysis of the monometallic palladium particles revealed a dependence of syngas production on nanoparticle size. The peak and steady state TOFs increased roughly linearly with the average nanoparticle diameter. The amount of coke deposited on the particle surfaces was found to be independent on the size of the nanoparticles. Shape control of the nickel-palladium nanoparticles with a high selectivity for (100) and (110) facets ($\leq$ 80%) has been demonstrated. The resulting alloy nanoparticles were found to have homogeneous composition throughout their volume and maintain FCC crystal structure. Substitution of Ni atoms in the Pd lattice at a 1:3 molar ratio was found to induce lattice strains of ~1%. The Ag nanocubes synthesized exhibited behavior very similar to literature values, when taken on their own, exhibiting a pair of distinct absorbance peaks at 350 nm and 455 nm. In physical mixtures with the Pd nanoparticles synthesized, their behavior showed that the peak position of the Ag nanocubes' absorbance in UV-Vis could be tuned based on the relative proportions of the Ag and Pd nanoparticles present in the suspension analysed. The Ag polyhedra

synthesized for comparison showed a broad doublet peak throughout the majority of the visible range before testing as a component in a physical mixture with the Pd nanoparticles. The addition of Pd nanoparticles to form a physical mixture resulted in some damping of the doublet peak observed as well as a corresponding shift in the baseline absorbance proportional to the amount of Pd added to the mixture.

Chapter 1: Introduction

1.1. Motivation and Objectives

The motivation behind this work has its roots in several different aspects of the current research into the shape control of nanoparticles synthesized for catalytic and sensing applications. Control of nanoparticle shape has the effect of allowing for the selective preparation of crystallites with specific atomic planes at the particle surface. Through the use of ions or capping agents during the synthesis of the nanoparticle catalyst, specific surface planes can be selected for[40-46]. By selecting for specific surface planes during the synthesis procedure, the catalytic properties of the nanoparticles formed can be tuned to allow the reaction under consideration to run more quickly by increasing the prevalence of available active sites. This bottom-up synthesis strategy can also be applied in the development of nanoparticles for SPR and magnetic sensing applications[47] as a result of the influence of nanoparticle shape on their optical properties.

Currently, as is well known, there is a search for economical and reliable methods of producing renewable energy. The primary driving force behind this search is the fundamentally finite nature of the use of existing fossil fuel deposits for the generation of energy. This has led to the investigation of a wide variety of different technologies, including solar cells, geothermal energy, fuel cells, and hydrogen generation. None of these technologies is truly mature yet, however. There are a wide variety of problems that

must be addressed before their implementation in place of fossil fuels is viable. The cost is perhaps the toughest barrier to overcome, though other issues such as efficiency and product lifetime also play important roles. The specific properties of the materials utilized then come into play. In catalytic applications, as in sensing, the material surface characteristics become extremely important.

In the work which will be discussed herein, the generation of hydrogen and synthesis gas (syngas) will be addressed as the primary focus of chapter 3. The catalysts that are currently most frequently used to generate hydrogen and syngas on a scale as is feasible for testing in a laboratory setting are synthesized from noble metals, such as platinum (Pt), and palladium (Pd). It is the rarity of these materials, and the cost of mining and refining them, which is a major factor limiting their widespread use in large scale industrial processes. The use of bimetallic Pt[1-15] and Pd[1-3, 5, 10, 11, 13, 15-38] catalysts, which combine one of the two metals with a second, more widely available, metal, has been investigated in recent years. Popular choices of bimetallic catalysts to investigate include Pt-Pd[2, 3, 5, 10], Ni-Pt[4, 6, 8, 9, 11-13, 39], and Ni-Pd[11, 13, 23, 25, 28, 31, 33, 34].

Size control of the synthesized nanoparticles has been shown to provide a mechanism which can be used to tune the optical properties of photocatalysts and nanoparticles synthesized for applications in luminescence enhancement, as well as their catalytic properties. In the preparation of cubic Ag nanoparticles, it has been shown that a particle size of greater than 50 nm gives the highest response[48-50]. A wide variety of catalytic reactions have been shown to proceed with rates corresponding to the size of the nanoparticle catalyst[46, 51-61].

Methanol dry reforming and methanol decomposition were used as model reactions for the production of hydrogen in the work presented herein, as well as for the production of syngas, as both products can be formed through these reactions. The effect of Pd nanoparticle size on catalytic activity in both reactions has not yet been established in the literature.

Similarly, the effects of shape and size of NiPd nanoparticles on their properties as sensor materials have not been investigated in depth in the literature. Ni particles have been used in biosensing applications such as the detection of acetaminophen[62] and cancer cells[63]. However, there is not yet a clear methodology for the synthesis of shape-controlled bimetallic NiPd nanoparticles in the literature. A synthesis procedure for the fabrication of shape-controlled NiPd nanoparticles will therefore be developed, in order to allow for the determination of the relationship between the nanoparticles' morphology and their behavior as sensing materials.

Ag and Pd nanoparticles were tested for their optical properties, for potential applications in sensing and plasmon-aided photocatalysis. Ag has been shown to be sensitive to incident photons, resulting in the oscillation of surface electrons and the re-radiation of the imparted energy as light through the generation of surface plasmons. This effect can be used to advantage in the development of highly sensitive analysis techniques such as Surface-Enhanced Raman Scattering (SERS) and biomedical applications such as biosensing[64-66], and immunoassays[67].

1.1.1. Objectives

The objectives of this work can be stated to be as follows in the context of the current state of the field:

- To determine whether the methanol decomposition reaction is structure sensitive when Pd nanoparticle catalyst is used, with and without co-fed CO_2, with the long-term goal of using the knowledge gained to improve existing industrial catalysts for the production of syngas.

- To develop a synthetic procedure based on the polyol technique to synthesize shape-controlled nanoparticles with bimetallic NiPd composition, because shape control of bimetallic nanoparticles has not yet been investigated in detail in the literature and the knowledge of how to achieve this would advance efforts to lower the cost of producing bimetallic nanoparticles for applications in catalysis or nickel-based biosensors.

- To elucidate the effects of physically mixing monometallic nanoparticles on the location and intensity of the observed surface plasmon resonances. This is envisioned as a step toward the long-term goal of producing finely tuned SPR biosensors. Scaling up a monometallic synthesis may be simpler than a bimetallic synthesis and still may maintain a high degree of homogeneity in the nanoparticles produced.

1.1.2. Hypotheses

Three hypotheses will be tested, each correlating with one of the stated objectives.

- Hypothesis 1: The methanol decomposition reaction will show increased turnover frequency as the diameter of the Pd nanoparticles used increases. Further, the size of nanoparticles synthesized can be tuned through the use of Pd precursors with different oxidation states by taking advantage of the difference in the reduction temperatures of the precursors and the associated nucleation rates.

- Hypothesis 2: Ni-Pd nanoparticles with shape control can be synthesized using a modified polyol procedure. Cubic and rod-shaped nanoparticles will be formed with higher frequency than polyhedral particles when using capping agents in the synthesis which favor the stabilization of (100) and (110) surface planes in monometallic syntheses of both Ni and Pd.

- Hypothesis 3: The location and intensity of SPR peaks generated by Ag nanocubes, Ag polyhedra, and Pd nanoboxes, respectively, will be affected by nanoparticle size and relative concentrations when combined into physical mixtures. It is expected that Ag nanocubes will generate a higher response than Ag polyhedra.

1.2. Background and Significance

1.2.1. Polyol Synthesis

A polyol synthesis is a procedurally simple methodology used to make nanoparticles. It is possible to ensure that the nanoparticles synthesized are of uniform size, shape, or composition, as needed, through the addition of stabilizing agents, as well as through the careful control of the synthesis conditions. The name of the technique originated as a result of the particular chemistry involved. A polyol is a compound that contains multiple hydroxyl (-OH) functional groups. The polyol is generally used as a solvent in the synthesis, and must be carefully chosen to solvate the metal precursors used. Ethylene glycol (EG) and 1,5-pentanediol are frequently used. The metal precursors are generally metal-organic compounds that decompose when heated, freeing the metal atoms they contain, thus allowing the metal atoms to diffuse through the polyol solvent and coalesce at available nucleation sites. In order to stabilize the metallic nanoparticles formed, a polymeric capping agent is sometimes added, to enhance the stability of the nanoparticles in solution and prevent agglomeration. A commonly used capping agent is poly(vinyl pyrrolidone) (PVP).

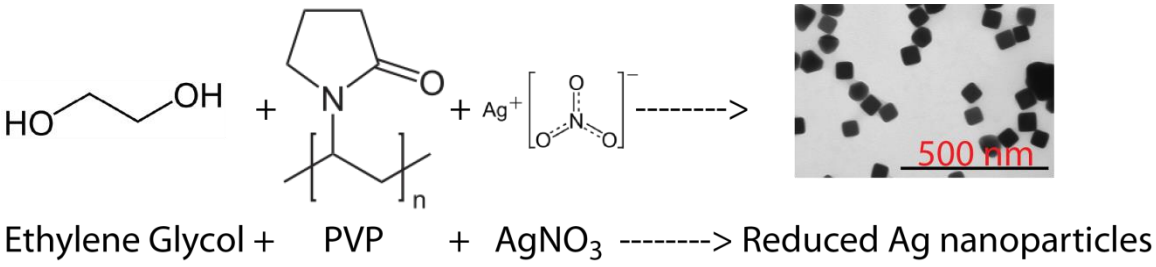

Figure 1: Schematic representation of a polyol synthesis for the production of Ag nanoparticles.

The combination of the concentration of metal precursors used, the reduction temperature set for the synthesis, and the concentration of the capping agent allows for control over the size and composition of the formed nanoparticles[1-3]. In order to control the shape of the nanoparticles, other compounds must sometimes be added to the synthesis. These vary widely based on the composition of the nanoparticles that are being synthesized and the desired shape. For example, it was reported by Harris that spherical Pt nanoparticles became nanocubes when the sample was exposed to H_2 gas containing a trace amount of H_2S[4]. In the case of Ag nanoparticles, Cl^- ions are generally preferred[5, 6]. The surface planes of a nanoparticle catalyst are defined as those crystal planes present at the surface of the particle, and are a function of the shape of the

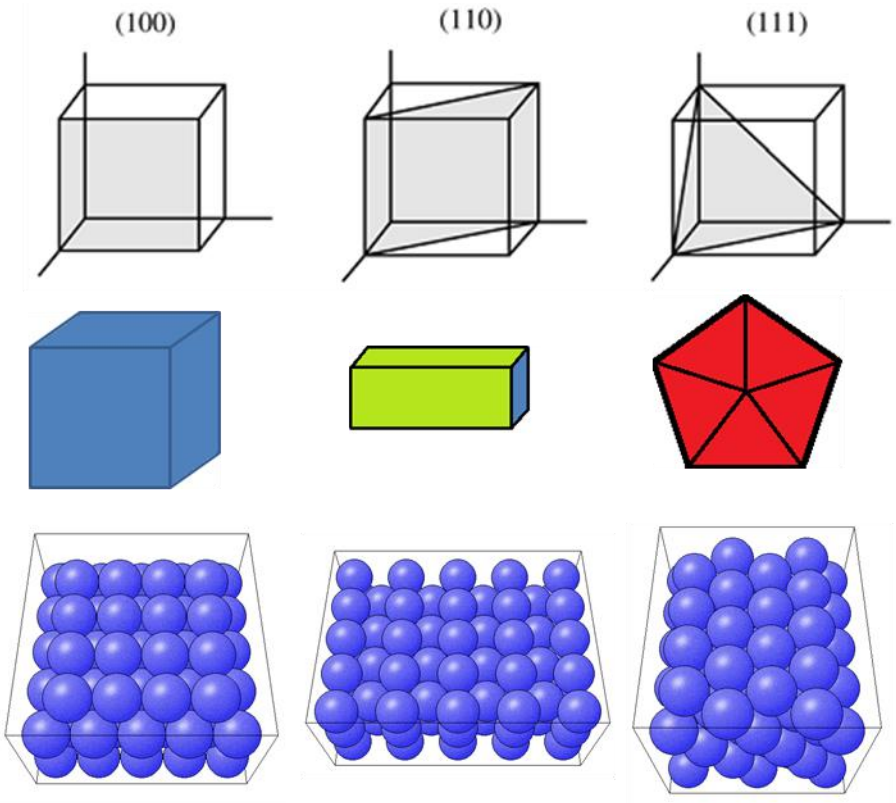

Figure 2: Surface planes of differently shaped nanoparticles. (100) faces are in blue, (110) faces are in green, and (111) faces are in red.

nanoparticle. In the case of a cubic particle, for example, the surface planes would all be (100) planes.

A number of models have been developed to describe the synthesis of nanoparticles in solution through wet chemistry methods such as the polyol method. One of these is the La Mer model, as presented in Figure 3. The La Mer model consists of three phases of crystal growth: (i) induction, (ii) nucleation, and (iii) growth. In phase one, the concentration of reactant atoms rises steadily with time until it reaches supersaturation levels, which are essential for nucleation. Once the solution's saturation point is reached, phase two begins and spontaneous nucleation occurs. The spontaneous nucleation events continue until the solution concentration dips back below the saturation point, at which point phase three begins and the nanoparticles formed enter the growth stage. In addition to the critical reactant concentration which is required for particle

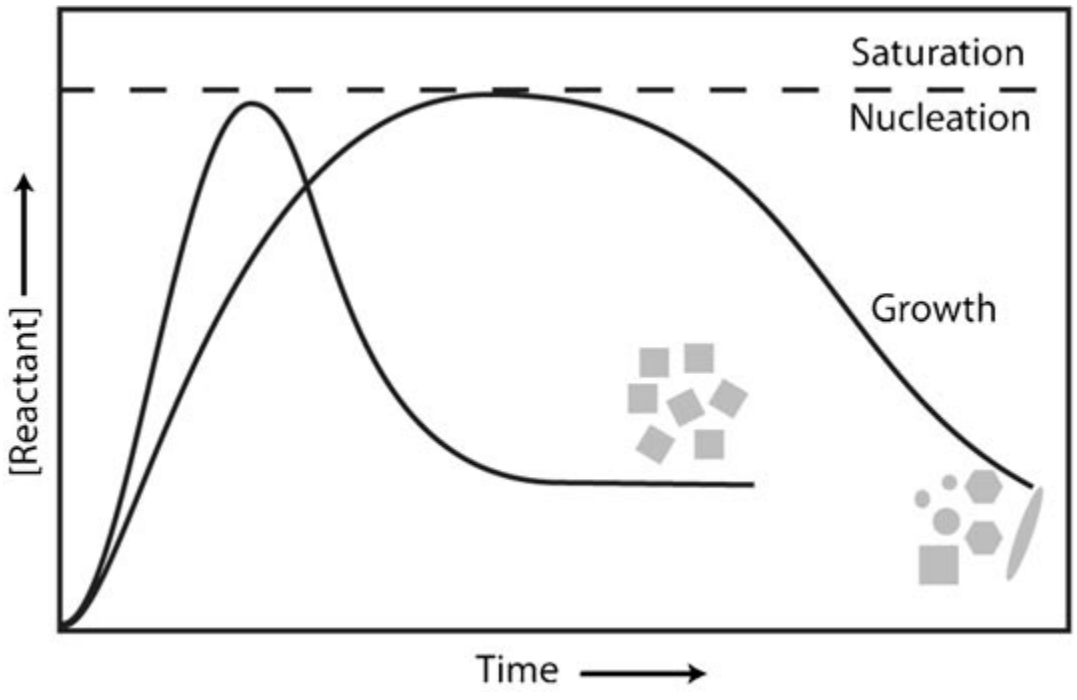

Figure 3: Generalised representation of the La Mer model of nucleation. Reprinted with permission from reference [6]. Copyright 2008 John Wiley and Sons.

nucleation, for the formation of homogenous nanoparticle morphologies a single, rapid nucleation event is needed.

The morphologies of the nanoparticles produced can be described as a function of the relative growth rates and energies of the low-index facets of the material in use. Using the example of a material with an FCC (face-centered cubic) crystal structure possessing a cuboctahedral shape, the surface facets present are of the {100} or {111} planes. The final nanoparticle morphology will depend on whether the growth of {100} or {111} facets is favored under the synthetic conditions used. These growth rates can be controlled through the use of specific capping agents or solvated ions[7-14]. For example, it has been shown in the literature that single crystalline Ag seeds grow to different shapes depending on the binding strength of the capping agents used[15, 16].

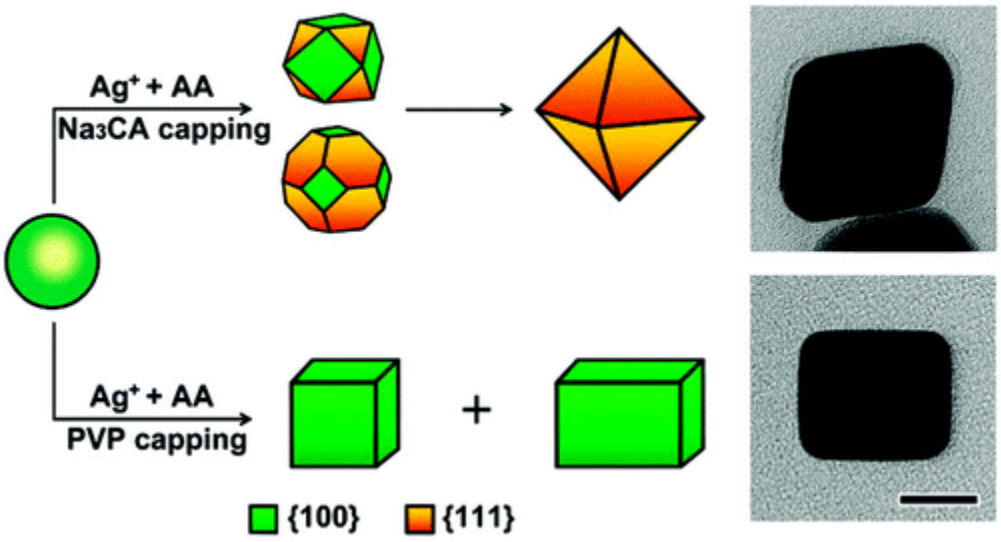

Figure 4: Effect of synthesis conditions on surface facet growth rate. Reprinted with permission from reference[15]. Copyright 2010 American Chemical Society.

The synthesis of hollow nanoparticles is also possible using this methodology, as a result of phenomena such as selective chemical etching, template-mediated synthesis,

and the Kirkendall effect[16]. In selective chemical etching, the etchants are used to selectively remove specific elements of the nanoparticles or facets through chemical reactions. Template mediated synthesis can be subdivided into two types: (i) core-shell syntheses, where the template remains intact, and (ii) sacrificial template mediated syntheses, where the template is partially or completely dissolved, typically with a redox reaction. If both components involved are metals, the process is termed galvanic displacement or electroless plating, as the process is primarily driven by the differences in standard electrode potential of the respective metals. The less noble metal serves as a presynthesized template and is oxidized under the loss of electrons, resulting in its dissolution[17]. This process has been taken advantage of by research groups to create hollow nanoscale materials[18-20].

1.2.2. Active Site Correlation with Surface Planes

A given catalytically active material, be it metal or oxide, will have surface active sites. The active site that is ‘seen’ by a given chemical reaction that can be driven with said catalytically active material differs from one reaction to another. The number of surface sites available will also vary based on the exposed crystal planes at the surface of the material. Crystal planes have differing atomic packing factors, and, as a result, a differing electronic structure and also differing numbers of sites with the correct electronic configuration to drive the reaction being studied. Thus, the shape of the synthesized nanoparticles will have an impact on their activity and selectivity toward a reaction of interest[21-28].

1.2.3. Surface Plasmon Resonance (SPR)

Surface plasmons are electromagnetic waves that propagate along the surface of a metal. Surface plasmons are very sensitive to changes in the dielectric constant of the environment the metal is in contact with. This applies to very localized variations, such as the adsorption of a molecule on the metal surface, as well as to macroscopic changes, such as putting the metal under high vacuum. In the case of a metal nanoparticle, surface plasmons can be excited by incident light, and the intensity of the surface plasmons can be enhanced by tuning the wavelength of the incident photons to the resonance wavelength of the metal. This frequency can be determined using UV-Vis spectroscopy in the form of absorbance peaks. Where the metal particles absorb light the most efficiently, the most surface plasmons will be generated. The position of the absorbance peak for metal nanoparticles can be tuned by changing the size, shape, and composition of the nanoparticles[11, 29]. Most metals show little or no plasmonic activity. The coinage metals gold (Au), silver (Ag), and copper (Cu), show the highest activity, though other materials can be used.[10, 11, 30-33]

1.2.4. Ni-Pd Size and Shape Effects

Shape control of nanoscale catalysts is important in determining their activity and selectivity. The crystal faces present at the nanoparticle surface determine the number and type of active site that the catalyst has. This phenomenon has been established experimentally in the case of Pd catalyst[34-36]. It has been demonstrated that the synthesis of shape controlled Pd nanoparticles with a narrow size distribution and high percentage of the desired shape can be achieved using polyol synthesis in combination

with a stabilizing agent[37, 38]. Choo *et al.*[39] showed that by slightly changing the synthesis conditions, the specific nanoparticle shape obtained could be changed. Further, the molar ratios of the precursor salt to the polymer, the reducing agent used, and the synthesis temperature, among others, were all factors influencing the outcome of the synthesis. As cited in the review by Tao *et al.*[6], the polymer PVP has been shown to act as an excellent shape control agent for such metals as Ag[6, 14, 40-42], Au[40, 41], and Pt[43, 44], among others. Others have shown that PVP can be used in the synthesis of shape-controlled Pd nanoparticles, as well[34, 35, 38, 42, 45].

To achieve shape control of Ni nanoparticles, a variety of approaches have been used, including wet chemistry techniques[46-52]. The main factors influencing the size and shape appear to be a combination of pH, reduction temperature, solvent, and precursor concentration. As cited in the review by Semagina and Kiwi-Minsker[53], Ni nanocubes have been synthesized by Telkar *et al.*[54] using ethanol as a reducing agent in the presence of a polymeric stabilizing agent, such as poly(vinyl pyrrolidone) (PVP), or poly(vinyl alcohol) (PVA). Bimetallic Ni-Pd nanoparticles have also been previously synthesized by the polyol method[55, 56]. However, while synthesis techniques for a variety of alloys of precious metals have been investigated[57], including Ni-Pt bimetallic nanoparticles[58], shape controlled Ni-Pd bimetallic catalysts have not. Additionally, size control of Ni[51, 59-66] and Pd[38, 67, 68] nanoparticles can be achieved through careful control of the synthesis conditions[67].

The shape of the nanoparticles determines the nature of active sites present and available for use in a reaction, and thus also the kinetics of the reaction. Since each catalyzed chemical reaction has a different active site, each reaction will therefore also

have a preferred crystal face on which it proceeds the most quickly. It has been shown in the literature that a Ni-Pt alloy will segregate under oxidizing conditions[69]. The different low index planes of Pt have been shown to have differing kinetics in the HCOOH oxidation reaction[70]. The low index crystal planes of Pd, on the other hand, have been tested in the oxygen reduction reaction[71, 72] and demonstrated to have different properties based on their surface crystal planes. Ni activity in methanol decomposition has been studied with DFT by Zhou *et al*[73]. They found that the mechanism by which the reaction proceeds varies for different low index planes, suggesting that the reaction is structure sensitive. Based on these results, a change in activity is expected for different shapes of synthesized Ni-Pd bimetallic particles.

1.2.5. Ni-Pd Segregation

Ni-Pd layer segregation through Low Energy Electron Diffraction Spectroscopy (LEEDS) shows that Pd is on the surface and Ni is in the second layer under vacuum.[74] Further, LEEDS also shows that for both the Ni-Pd(100) and Ni-Pd(111) planes the composition is oscillatory, with the outermost layer containing mostly Pd and the next Ni[75, 76] as is predicted through surface energy and bond-breaking arguments[76]. Based on the DFT calculations and experimental results of Menning *et al.*[77] the segregation of a transition metal such as Ni or Co to the surface of a Pt-M-Pt (111) or (100) plane is thermodynamically favored in the presence of oxygen. This result is likely to hold for Pd as well, given the similarities of their properties. Further, under reaction conditions, the catalyst particles are likely to segregate more due to external forces in the form of adsorbates, oxidizing agents, or reducing agents, rather than due to the properties

of the metals themselves. The adsorption-induced segregation behavior of Ni-Pd alloy particles is not clearly described in the literature. Most experimental studies that address surface segregation are done under high vacuum prior to or without catalytic testing[74-76, 78-80], and thus eliminate any influence adsorbates would have on the system under reaction conditions. Helfensteyn *et al* found, through a theoretical study using Monte-Carlo simulation methods, that Pd atoms became surface segregated[81]. Løvvik[82] performed a DFT band-structure study whose results were in good agreement with those of Helfensteyn *et al*. Their results do not take into account adsorbate effects, however. Menon *et al*.[83] did a computational study that showed Ni atoms were surface segregated in the presence of oxygen. Ma et al.[84] did a computational study on Pt3Ni that showed that there was no segregation of metals with a ¼ monolayer coverage of oxygen. Menning and Chen have calculated using DFT that the thermodynamic potential for surface segregation increases with the Pauling electronegativity for a group of selected adsorbates[85]. No studies have been found on the effects of size and shape on adsorption-induced nanoparticle segregation effects on Ni and Pd. This information would be instrumental in helping refine our knowledge of how a bimetallic catalyst's activity and selectivity are influenced by composition.

1.2.6. Ag-Pd Nanoparticles

Ag nanoparticles have been found to significantly enhance Raman scattering as a result of their higher polarizability relative to bulk materials [30]. The nanoparticles effectively act as antennae to 'focus' incident light on the sub-wavelength scale. This makes possible the sensitivity increase of 10^6 seen in surface-enhanced Raman scattering

(SERS) relative to conventional Raman scattering. Nanoparticles of suitable size and composition to detect single molecules have been demonstrated[31]. The sensitivity increase is dependent on the size of the nanoparticles used. For nanoparticles of 30nm and more in diameter, the amount of incident light that is absorbed is much larger than the amount of scattered light. For particle sizes of less than 30 nm in diameter, more light is scattered than absorbed.

The synthesis of Ag nanoparticles for use in such applications can be done in a variety of ways, including the polyol synthesis[14, 42, 86, 87]. The shape of the nanoparticles synthesized in such a manner is generally controlled through the use of a polymeric capping agent[12, 86] or solvated halide ions such as Cl^{-}[6, 86] and Br^{-}[14, 86].

Pd nanoparticles have not been as popular for such applications because they exhibit a low broad absorbance peak throughout the range of the near-infrared, visible, and near-UV portions of the light spectrum[1], rather than a sharply defined peak over a narrow range of wavelengths. As a result, it is not easily possible to tune the wavelength of the incident light such that the energy is efficiently converted into a usable form. For metals, such as Ag or Au, that have a sharply defined absorbance peak, the wavelength of the incident light can be adjusted such that more of it is used effectively. Bimetallic nanoparticles have been shown to make highly sensitive biochemical sensors[88, 89], and hydrogen sensors[90-92]. The size and shape of the particles allows the position of the narrow absorption band to be tuned[1, 6, 30, 40, 45, 86, 93]. As shown by Si et al[32], as the size of the silver particles synthesized decreases, their absorbance peak is blue-shifted. However, as the size of the particles was reduced, the shape distribution changed, with the larger particles having a very uniform size and shape, and the smaller particles

having spheres and truncated polyhedra present in addition to those particle shapes desired. Chen *et al*.[94] synthesized Ag nanoparticles of differing shapes and investigated their optical properties using UV-Vis spectroscopy. It was found that the shape has a profound effect on the nanoparticles' absorption, with the nanocubes exhibiting a broad absorption peak that spanned most of the visible range, between wavelengths of 400 and 750nm. The synthesized nanospheres had a sharper absorption peak at a wavelength of 440 nm, and the nanoplates also showed a broad absorption peak throughout the visible range, but with roughly half the absorbance of the nanocubes. Thus, in order to achieve optimal conversion of incident radiation into surface plasmons, the best particle shape to use, of those studied, would be a cube. Lu *et al*.[10] performed a similar study, using nanocubes and nanobars to study the effect of aspect ratio on the absorption peak, finding that a higher aspect ratio resulted in a red-shift of the absorption peak.

The addition of Pd to Ag nanocubes shifts the absorption peak. Lee *et al*.[95] synthesized hollow Ag-Pd nanoparticles using a displacement reaction, and found that though monometallic Pd nanoparticles did not show an absorbance peak, the hollow bimetallic particles did. The absorbance peak of the bimetallic particles was red-shifted, relative to the absorbance peak of the monometallic Ag nanoparticles synthesized, and less intense. Chen *et al*.[19] synthesized Ag-Pd nanoboxes with varying amounts of Pd added to Ag nanocubes in solution. UV-Vis analysis showed that the more Pd was added, the more the absorbance peak was red-shifted.

These bimetallic nanoparticles have been used in the design of novel biosensors[88, 89, 96]. By tuning the absorbance peaks of the nanoparticles used and increasing their sensitivity to changes in the dielectric interface at their surfaces, the

efficiency and applicability of nanoparticles as sensors is improved. Thus, by combining the effects of composition, shape, and size, it is predicted that cubic Ag-Pd nanoparticles with high sensitivity and well-defined absorbance peak can be synthesized.

1.2.7. Ni-Pd Composition Effects

A recent review on the effect of the physical and chemical characteristics of a catalyst on its activity[93] was done by Cuenya, citing changes in catalyst activity based on size, shape, composition, oxidation state, and support effects. In the case of Pt catalyst, it has been shown that by alloying with other metals, such as Fe, Ru, Ni, and Co, among others, the catalysts formed show enhanced hydrogenation activity[97-100]. Moreover, recent theoretical and experimental studies done by Chen's group[100], show that a Pt-Ni-Pt structure has superior hydrogenation activity compared to Ni-Pt-Pt. They found that the presence of Ni atoms at the surface of layered catalysts induced a shift in the d-band towards the Fermi level, resulting in a stronger surface-adsorbate interaction. By contrast, when the Ni atoms were subsurface, the opposite trend was observed.

Due to the chemical similarities between Pt and Pd, similar trends can be expected to be exhibited by synthesized catalyst, and indeed, in reactions such as the oxygen reduction reaction (ORR) which is of paramount importance in such areas as fuel cell research, the transfer of electrons from the adatoms of the alloying metal to the Pd to fill the d-band decreases the density of states (DOS) at the Fermi level[101]. This change in the DOS affects the adsorption strength of O and OH species on the catalyst surface, effectively lowering it. This in turn decreases the likelihood that Pd oxide species will form on the catalyst surface, allowing its activity to be maintained. Similarly, the

composition of the Pd alloy particles has an effect on their activity[56, 102-104]. For example, it was shown by Singh *et al*.[103] that the dependence of hydrogen selectivity in the decomposition of hydrous hydrazine varied with the ratio of Ni to Pd used in their catalyst, with the highest selectivities being achieved at compositions containing between 35%-45% Pd.

Chapter 2: Analysis Techniques

2.1. Transmission Electron Microscopy (TEM)

TEM is an imaging technique similar to light microscopy, but which uses electrons as its source of illumination, rather than photons. The advantage of using electrons is that they have a far greater resolving power than photons, due to their much shorter wavelengths. The resolving power of a microscope is defined by the wavelength of the source of illumination, as in equation 1, where d is used to denote the maximum achievable resolution.

$$d = \frac{\lambda}{2 * (numerical\ aperture)} \qquad \text{Eq. 1}$$

In the case of a light microscope, the resolving power is limited by the wavelengths visible to the human eye. This is not the case when using electrons for illumination, as the electrons' wavelength can be tuned by changing the accelerating voltage used. The higher the accelerating voltage, the shorter the electrons' wavelength, and thus the higher the achievable resolution. When electrons are used, however, other methods of displaying the image are necessary, such as a phosphorus screen or a CCD camera. Further, in order to use electrons for imaging, the sample must be placed under vacuum and be prepared in such a way that it is transparent to the electrons. For most materials, this falls into the range of 50-200 nm.

2.2. X-Ray Diffraction (XRD)

XRD is an analytical technique used to identify materials and crystal structures. Bragg diffraction is most commonly executed, as it allows for the investigation of three dimensional lattice structures. Bragg diffraction takes advantage of the constructive and destructive interference of electromagnetic waves being reflected by the crystal planes present in a single crystal or powder sample. The condition that must be satisfied for constructive interference to occur is given by Bragg's Law:

$$n\lambda = 2dsin\theta \qquad \text{Eq. 2}$$

If a non-integral number of oscillations of the electromagnetic field occur between crystal planes, the diffracted x-rays interfere destructively. The distance that the x-rays must travel is determined by the interplanar distance (d), and the angle of incidence (θ).

Essentially, the peak position in degrees (θ) corresponding to a given crystal plane is determined by the wavelength of the incident x-rays (λ), and the interplanar distance (d). This allows for accurate determination of composition due to the high degree of sensitivity to changes in lattice parameters from element to element. Further, each type of crystal structure has a characteristic set of 'allowed' reflections. Not all crystal planes present in a sample will generate a diffraction peak as a result of the structure factor of the lattice[105]. For example, in the case of a face-centered cubic material, only crystal planes having either all odd indices (e.g. (111), (311)), or all even indices (e.g. (200), (222)), will be observed.

2.3. Energy Dispersive X-ray Spectroscopy (EDS or EDX)

EDX is used to determine the elemental composition of a sample. As a result of the quantized nature of the energy levels of electron orbitals, it is possible to determine what elements are present in a sample by exciting their electrons. The electrons are excited using x-rays of high enough energies to ionize the atom by removing an electron from one of the core orbitals. This, in turn, causes an electron from a higher orbital to drop down to fill the hole created. When this occurs, an x-ray of characteristic energy is emitted. The energy of the emitted x-ray is a specific to the element and the orbital transition occurring. EDX can also be used to determine the locations of specific elements within a sample through the use of techniques known as elemental mapping and line-scanning.

2.4. Ultraviolet-Visible Spectrometry (UV-VIS)

UV-VIS spectrometry is used to determine the wavelengths of light, ranging from 190nm - 1200nm, that a sample absorbs. The wavelengths absorbed correspond to the quantized energies required to induce electrons to transition from an occupied orbital to an unoccupied one. In the case of molecules, the most common such transition is from the highest occupied molecular orbital (HOMO) to the lowest unoccupied molecular orbital (LUMO). When working with optically active metals, such as silver, the wavelengths at which the material absorbs light correspond to the wavelengths at which other phenomena, such as localized surface plasmon resonance, occur.

2.5. Mass Spectrometry (MS)

Mass spectrometry is used to identify molecules and measure concentrations, and is, at its most basic level, comprised of three steps. First, the molecules to be analyzed are bombarded with high energy electrons in order to ionize them. The ionized molecules are then separated according to their mass-to-charge ratios (m/z) using a magnetic or electric field. The electric or magnetic field is also used to accelerate the molecules toward the detector, and can be adjusted such that only molecules with a specific mass-to-charge ratio are striking the detector at any given time. The resulting signal is amplified and then recorded, generally using a computer.

MS can be used to analyze a wide variety of sample types. The studies presented in subsequent chapters are based on the analysis of gas-phase chemical reactions. When used in combination with a flow system and a furnace, catalytic systems can be studied in detail. The use of a flow system allows for fine control of the gases flowing over the catalytic material being studied, and the furnace enables control of the temperature at which the reaction is occurring. In essence, by studying the changes between the inlet and effluent streams, the activity of the catalyst can be observed and quantified. In the study of catalytic materials, three temperature-dependent techniques are commonly used.

2.5.1. Temperature Programmed Reduction (TPR)

Temperature programmed reduction is used primarily to determine the degree of oxidation of a catalyst sample. In some cases, only the reduced metal atom is catalytically active, and the oxide phase is not. In cases such as these, it is necessary to reduce the

catalyst before its catalytic properties can be determined. This is typically done by heating the catalyst sample under reducing conditions.

2.5.2. Temperature Programmed Reaction Spectroscopy (TPRS)

Temperature programmed reaction spectroscopy is commonly used to quantify the activity of a catalytic material in a given reaction. By adjusting the composition of the inlet stream to contain the reactants and monitoring the composition of the effluent stream, the conversion and reaction rate, among other parameters, can be calculated. When done in combination with the use of a furnace, the changes in catalytic activity with temperature can be quantified.

2.5.3. Temperature Programmed Oxidation (TPO)

Temperature programmed oxidation is typically used to determine the extent of carbon deposition on a catalyst sample (coking) post-reaction. The degree of coking can be quantitatively determined by heating the sample under oxidizing conditions, and subsequently integrating the area under the CO and CO_2 traces, as these are directly proportional to the amount of coke deposited on the catalyst surface.

2.6. X-Ray Absorption Spectroscopy (XAS)

XAS is a technique based on the same fundamental principles as EDX, but adds a second layer of complexity. By exciting a core shell electron with enough energy to create a vacancy, the absorbing atom is brought out of its ground state. This causes an electron from a higher orbital to drop down to fill the vacancy, and emit a photo-electron

with characteristic energy, as shown in Figure 5. The emitted photo-electron can be scattered by neighboring atoms, introducing what is known as a phase-shift. As a result, the scattering event can cause the photo-electron's wave function to interfere with itself. This interference varies with the energy of the incident radiation, causing oscillations in the probability that the incident radiation will be absorbed. As a result, the sample's valence state can be directly measured, and for crystalline structures information about coordination number can be gained through careful analysis of the data using Fourier transforms[106].

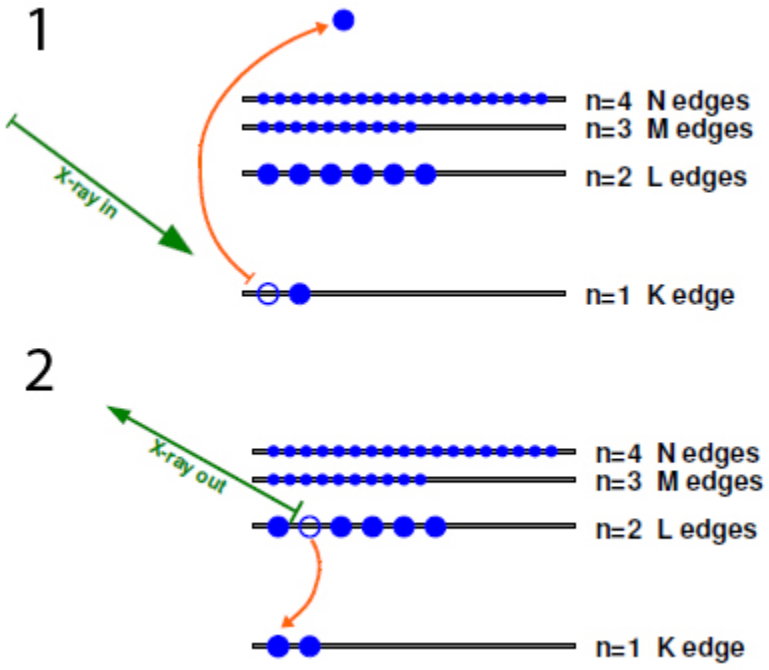

Figure 5: Principles of XAS.

Chapter 3: Role of Pd Nanoparticle Size in Methanol Decomposition Reaction

In this chapter, a detailed description of the methods used to synthesize and characterize size-controlled Pd nanoparticles is given. The first objective is to synthesize Pd nanoparticles with a narrow size distribution and support them on silica. This is achieved through use of a one-pot polyol synthesis and a controlled molar ratio of Pd(IV) and Pd(II) precursors. The nanoparticles synthesized using these techniques were supported on silica at 2%wt for TPR and TPO analysis as well as catalytic activity testing.

To determine the physicochemical and catalytic properties of the synthesized particles, a variety of characterization techniques will be used. In order to ascertain the physical characteristics of the nanoparticles -- size, shape, crystallinity, and atomic composition -- TEM, SEM, XRD, and UV-Vis spectroscopy will be utilized. The catalytic properties will be explored using temperature programmed techniques: TPR, TPO, and TPSR.

3.1. Experimental Details

3.1.1. Polyol Synthesis

The Pd(II) precursor Ammonium tetrachloropalladate (Formula: $(NH_4)_2PdCl_4$) and Pd(IV) precursor Ammonium hexachloropalladate (Formula: $(NH_4)_2PdCl_6$) were used in varying molar ratios as shown in Table 1. An excess of PVP (m.w. 40,000) at a

molar ratio of 40:1 relative to the moles of Pd metal was added to the Pd precursors, and then everything was dissolved in 10 mL of ethylene glycol. The solution was heated to 220°C under argon atmosphere and held at temperature for 20 minutes, as shown in Figure 6.

Table 1: Molar Ratios and Calculated mg Amounts of Pd(II) and Pd(IV) Precursors

Molar ratio of Pd(IV)	Pd(IV) precursor (mg)	Molar ratio of Pd(II)	Pd(II) precursor (mg)
0%	0	100%	14.2
20%	3.6	80%	11.4
40%	7.1	60%	8.5
60%	10.7	40%	5.7
80%	14.2	20%	2.9
100%	17.8	0%	0

The solution, initially a light yellow-orange color, turns black or dark brown, indicating that reduction of the precursors has taken place and a suspension of metallic Pd nanoparticles has formed. At the end of 20 minutes, the solution is allowed to slowly cool in the oil bath.

The particles are then precipitated with an excess (80 mL) of acetone. The supernatant is then removed, and the particles are resuspended in ethanol and washed three times, alternating hexane and ethanol to remove excess PVP. After washing, the particles are resuspended in 20 mL of ethanol.

3.1.2. Silica Support

The polyol synthesis described in Section 3.1.1 makes a batch of approximately 25.5 mg of nanoparticles, assuming all of the Pd contained in the precursors is present in the synthesized particles. Thus, 10 mL of the 20 mL ethanol suspension was combined

with powdered silica support (~200 m^2/g) and sonicated at room temperature for 60 minutes to produce a supported catalyst with a metal loading of 2% by weight.

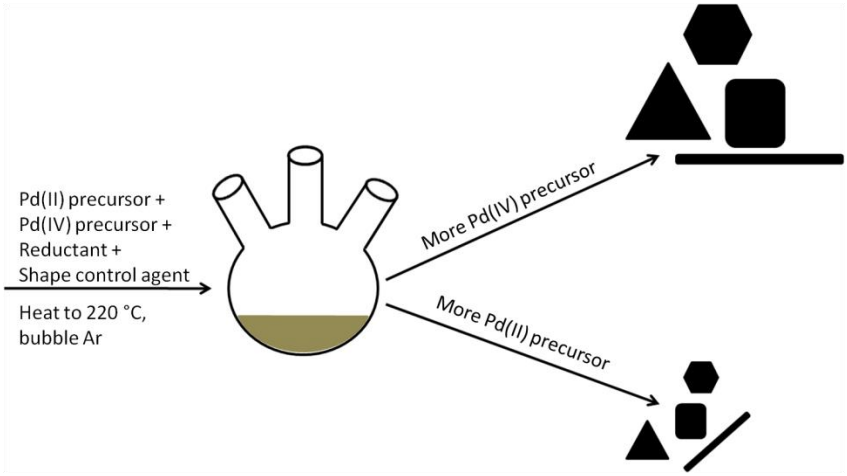

Figure 6: Schematic representation of the one-pot polyol synthesis method for fabricating monometallic Pd nanoparticles of controlled sizes. Adapted with permission from reference [107]. Copyright 2012 American Chemical Society.

The resulting slurry was centrifuged at 6500 RPM for 15 minutes, and the supernatant discarded. The resulting gel was dried and crushed into a fine powder for use in temperature programmed techniques.

3.2. Characterisation Techniques

Physical characterization of nanoparticles was done using XAS, TEM, and XRD. XAS was performed at DuPont-Northwestern-Dow (DND) Collaborative Access Team (CAT) beamline 5-BM-D (BM = bending magnet, http://www.dnd.aps.anl.gov/) at the Advanced Photon Source, Argonne National Laboratory using the procedures, including the Athena software package[108, 109], as described in Appendix 1. TEM and XRD were

performed on unsupported particles whereas XAS was conducted on the silica-supported particles. TEM samples were prepared by depositing a drop of nanoparticles suspended in ethanol on a carbon formvar grid (200 mesh, Electron Microscopy Sciences, PA), and measurements were performed on an FEI Morgagni 268D using an acceleration voltage of 60 kV. A Philips X'pert Pro materials research diffractometer was used to analyze the crystal structure of the synthesized Pd nanoparticles. Samples were prepared for XRD by drying the ethanol-suspended nanoparticles on a clean glass slide.

The catalytic properties and surface characteristics of the nanoparticles were ascertained using TPR, TPO, and TPSR. TPR was used to determine the amount of surface oxide formed on the nanoparticles during synthesis, based on the amount of hydrogen that is converted to water. TPO was used for two purposes: to calculate the amount of amorphous carbon accumulating on the nanoparticle surface during temperature programmed reaction studies on the dry reforming and decomposition of methanol, respectively, and to gain a preliminary understanding of potential size effects based on the temperature at which the PVP functionalized on the nanoparticle surface is combusted. TPSR was utilized to determine the catalytic properties, such as TOF, of the fabricated nanoparticles for methanol dry reforming.

The catalytic decomposition and dry reforming of methanol were done with a bench scale fixed bed quartz U-tube flow reactor placed in a Thermolyne tube furnace controlled by a type-K thermocouple. Calibrated mass flow controllers manufactured by Alicat Scientific were used to control the reactor inlet stream composition. Prior to catalytic testing, a pretreatment step was performed, during which the catalysts were exposed to a flow of 5 SCCM of oxygen and 45 SCCM of helium during a temperature

ramp from room temperature to 350 °C with a ramp rate of 10 °C/min and a 1 h hold. This step was done to remove excess capping agent and make contact between the inlet stream and the catalyst's active sites possible.

The total volumetric flowrate of the inlet stream was held constant at 76 SCCM for experiments run with and without carbon dioxide, respectively. In the absence of carbon dioxide, the inlet stream was comprised of 3.8 SCCM of methanol and 72.2 SCCM of helium. When carbon dioxide was introduced, the respective flowrates of the inlet stream components were 3.8 SCCM of methanol, 3.8 SCCM of carbon dioxide, and 68.4 SCCM of helium. In both sets of experiments, the inlet stream was introduced to the reactor at atmospheric pressure, and the composition of the effluent stream was analyzed in real time using a mass spectrometer (MKS Cirrus) with an electron multiplier detector. The reactions were studied using a temperature program increasing from room temperature to 350 °C at a ramp rate of 10 °C/min and incorporating a 2 h hold at 350 °C. The TOFs were determined for each size of nanoparticles by quantifying the conversion of methanol (from the m/z = 31) obtained under differential conditions, attained by adjusting the mass of catalyst used to limit the steady-state conversion to 15% or less. These results were then normalized per surface atom, using the dispersion calculated from the measured nanoparticle size, in order to correct for the surface-to-bulk ratio of the atoms contained in the nanoparticles.

Two different types of post-reaction experiments were performed. In the first type, the catalyst was cooled under helium, then the reaction step was repeated under the same experimental conditions. In the second, the catalyst was cooled under helium, then TPO was performed to measure carbon dioxide generation due to the combustion of coke

deposits. TPO experiments, performed using the same apparatus as described above in the reaction studies, used a flow of 5 SCCM of oxygen and 45 SCCM of helium. A temperature program from room temperature to 500 °C with a ramp rate of 10 °C/min and a 1 h hold at 500 °C was used, and the carbon dioxide signal (m/z = 44) was used to calculate the grams of coke deposited per gram catalyst.

3.3. Results and Discussion

XRD spectra were taken for all six ratios of precursor used in particle synthesis to verify that the particles formed are metallic. The results are plotted in Figure . The notation used gives the percent of the total precursor amount that is Pd(IV), with the balance being comprised of Pd(II) precursor. The peaks present are characteristic of metallic palladium, with no oxide peaks appearing, showing good agreement with JCPDS entry 46-1043. The peak positions for all samples, at (40.1°, 46.6°, 68.0°, and 82.0° 2θ) correspond to an FCC lattice with unit cell length 3.89 Å. Some peak broadening is observed, indicating that the nanoparticles synthesized are small. Typical TEM images of the six samples are shown alongside the plotted XRD spectra. Qualitatively, it is clear that the nanoparticle size increases with increasing Pd(IV):Pd(II) ratio. A statistical analysis confirms this observed trend. Pd nanoparticle sizes calculated from XRD data using the Scherrer equation (shown below) for each precursor ratio are plotted in Figure 8, with the corresponding average diameter calculated from TEM images.

$$D_{avg} = \frac{K\lambda}{\beta \cos\theta} \qquad \text{Eq. 3}$$

The Scherrer equation terms include the shape factor, K, x-ray wavelength, λ, full-width half maximum, β, and the Bragg angle in radians, θ. Very good agreement was

found between the calculated Scherrer diameter and the measured TEM diameter, with the Scherrer diameter values lying within one standard deviation of the measured values. As was expected, the standard deviation rose with increasing nanoparticle diameter, however, it remained below 35% of the mean measured diameter for all samples, indicating that the distribution of sizes remained narrow throughout the range synthesized.

The measured particle diameters in TEM and the calculated Scherrer diameters show the expected trend towards larger particles with increasing Pd(IV) content. It is worth noting that the Scherrer equation calculates the average crystallite size; given a polycrystalline material, this would yield the average grain size. In the case of single crystalline and isotropic materials, such as nanoparticle catalysts, the Scherrer equation

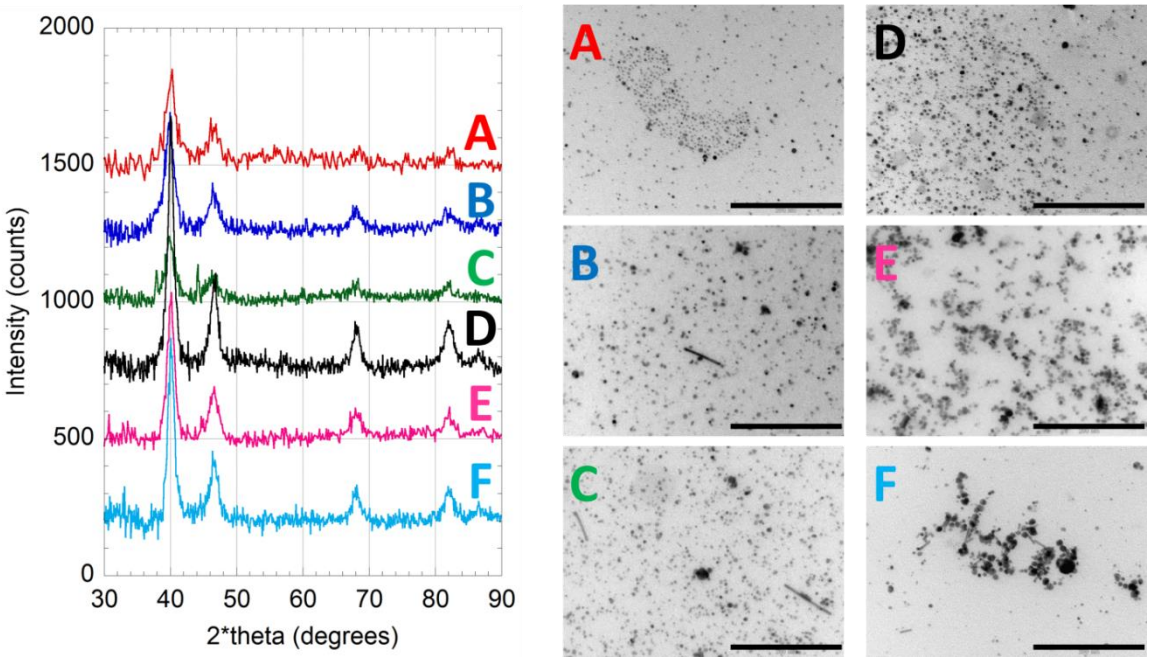

Figure 7: XRD spectra of Pd nanoparticles synthesized through the one-pot polyol synthesis. Precursor ratios of (A) 0%, (B) 20%, (C) 40%, (D) 60%, (E) 80%, and (F) 100% Pd(IV) are shown along with corresponding TEM images taken at 60kV and a magnification of 180kx. Scale bars represent 200nm.

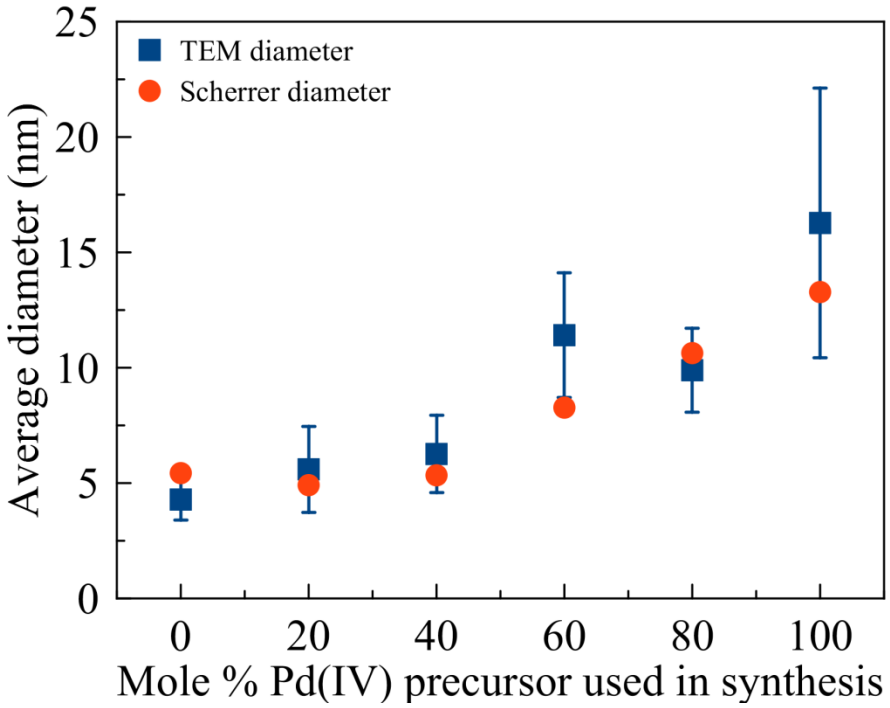

Figure 8: Average diameter measured in TEM and calculated Scherrer diameter of synthesized Pd nanoparticles. Reprinted with permission from reference [107]. Copyright 2012 American Chemical Society.

calculates the average particle size, assuming a spherical nanoparticle. It is evident from images taken with TEM that the assumption of a spherical particle does not hold for all samples, as shown in the images in Figure 7. As the observed particle size increases, so too does the proportion of polyhedral particles relative to the number of spherical ones.

Further, the calculations of the nanoparticle diameters using the Scherrer equation incorporate some error in the form of contributions to the XRD signal from agglomerated nanoparticles, whereas measurements taken from the TEM images do not, as any groups of agglomerated particles were not measured. As a result, the measured and calculated values do not exactly correspond.

After immobilization of the Pd nanoparticles on silica, XAS and catalytic characterization were done. In XAS results, both the XANES and the EXAFS regions

were shown to be characteristic of the metallic zero-valence state of the Pd. This indicates that the valence state of the nanoparticles was maintained, regardless of size. The lower intensity of the peak at 24365 eV relative to the first EXAFS region peak at 24390 eV, as shown in Figure 9, is indicative of a metallic nanoparticle, rather than a metal oxide. The presence of a metal oxide is observed in XAS as an increase in the relative intensity of the XANES region features relative to the EXAFS region intensity. This occurs as a result of the increase in oxidation state of the metal atoms due to the increased proximity of bonding atoms to said metal atom. This, in turn, results in an increase in the likelihood of multiscattering events[110]. Additionally, the observed

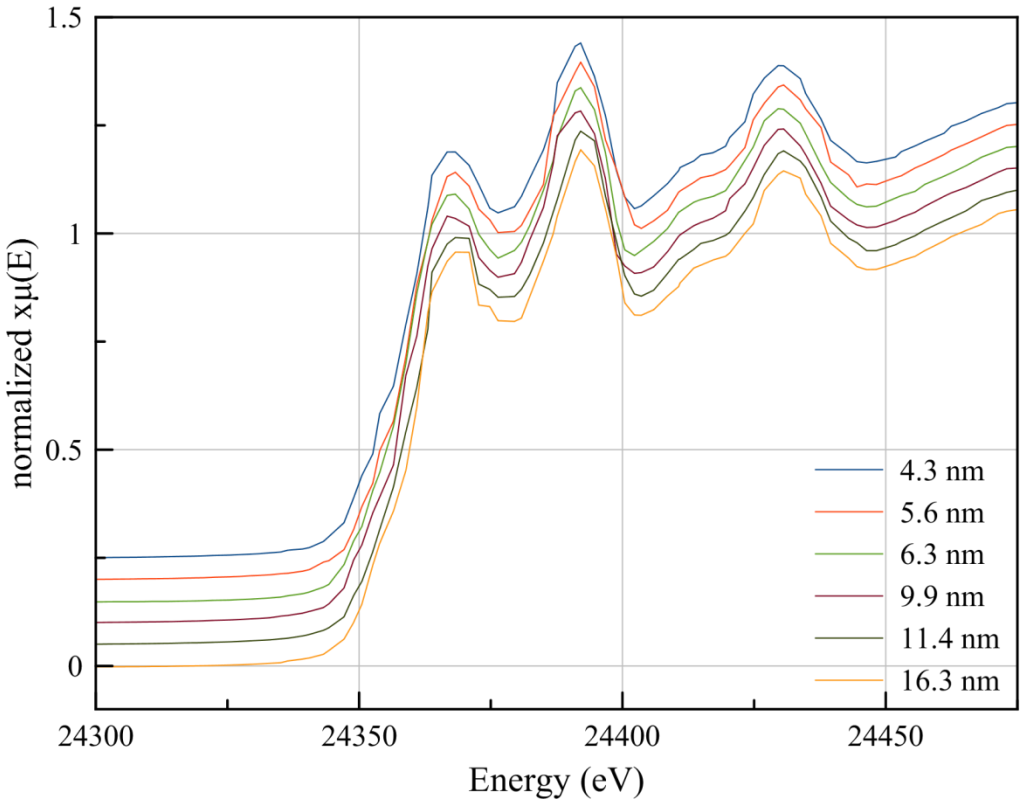

Figure 9: XANES region as a function of percentage of Pd particle size. Spectra are offset for clarity. Reprinted with permission from reference [107]. Copyright 2012 American Chemical Society.

resonance in the EXAFS region matches closely with that of the metallic Pd foil used as a reference.

Investigations of the catalytic properties of the synthesized catalysts using temperature programmed techniques of reduction (TPR), oxidation (TPO), and reaction (TPRS) were done on similarly prepared silica-supported samples. TPR results, not shown here, show that there was no appreciable amount of surface oxide on the particles, an observation supported by the absence of PdO peaks in the XRD spectra presented in Figure 7 Figure and the XAS results. The nanoparticles fabricated did not have a significant surface oxide layer, as there was no decrease in the amount of H_2 seen by the detector. TPO pretreatments done on each sample prior to running TPRS revealed that the amount of PVP present in each sample prior to reaction was approximately equal, based on the integrated areas of the CO_2 peaks observed, as would be expected given that the catalyst loading was held constant. The calculated values are given in Table 2.

In the catalytic studies performed, the methanol decomposition and dry reforming reactions (Eq. 4a and 4b, respectively) were run. Temperature programmed reaction tests run on the methanol dry reforming (MDR) reaction (Eq. 2b) over the supported Pd nanoparticles yields a trend in which the turnover frequency per Pd surface atom increases roughly linearly with the nanoparticle size, within the range studied, as shown in Figure 10 (inset).

$$CH_3OH \xrightarrow{yields} 2H_2 + CO \qquad \text{Eq. 4a}$$

$$CH_3OH + CO_2 \xrightarrow{yields} 2H_2 + CO + CO_2 \qquad \text{Eq. 4b}$$

It is interesting to note that once the reaction reaches steady state, the relationship between particle size and hydrogen production is linear and the amount of hydrogen

produced decreases with increasing particle size. Further, the only observed products were carbon monoxide (m/z = 28) and hydrogen (m/z = 2). No conversion of methanol was observed when using silica (with no Pd nanoparticles) as a catalyst under the same conditions.

For comparison, the same study was done using the largest and smallest particles in the methanol decomposition reaction. The peak and steady state TOF calculated remained comparable to those for MDR, indicating that the additional CO_2 flowed during

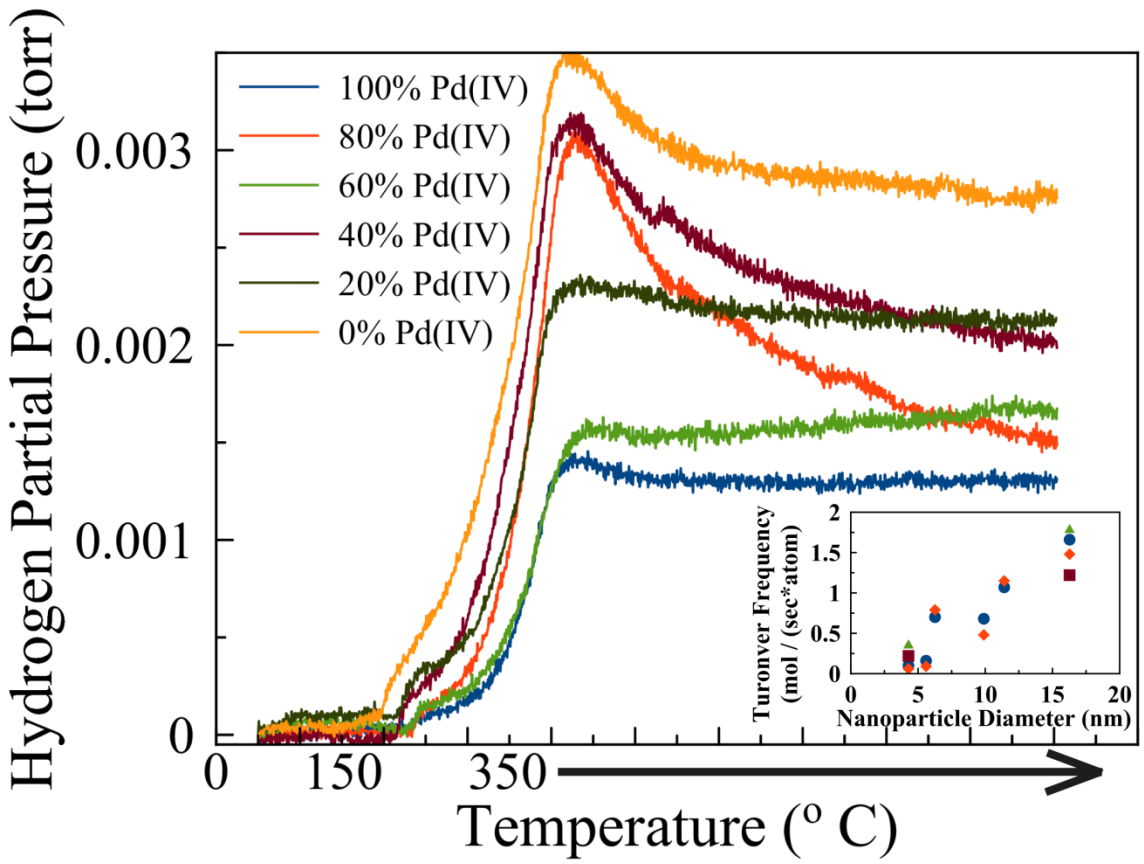

Figure 10: Hydrogen production during methanol dry reforming as a function of reaction temperature, and (inset) peak methanol conversion TOF versus particle size calculated in terms of mol sec-1 atom-1. Blue circles represent the peak TOF during the methanol dry reforming (MDR) reaction, orange diamonds represent the steady state MDR TOF. Similarly, green triangles and red squares represent the methanol decomposition peak and steady state TOFs, respectively.

the MDR studies did not greatly influence the reaction rate. As shown in Figure 11, the production of CO_2 does not follow the same trends as the hydrogen and carbon monoxide traces. The peak in the H_2 production corresponds to the peak reaction rate. At steady state, however, the amount of H_2 produced by a given sample correlates with the particle size, with the smallest particles generating the most gas.

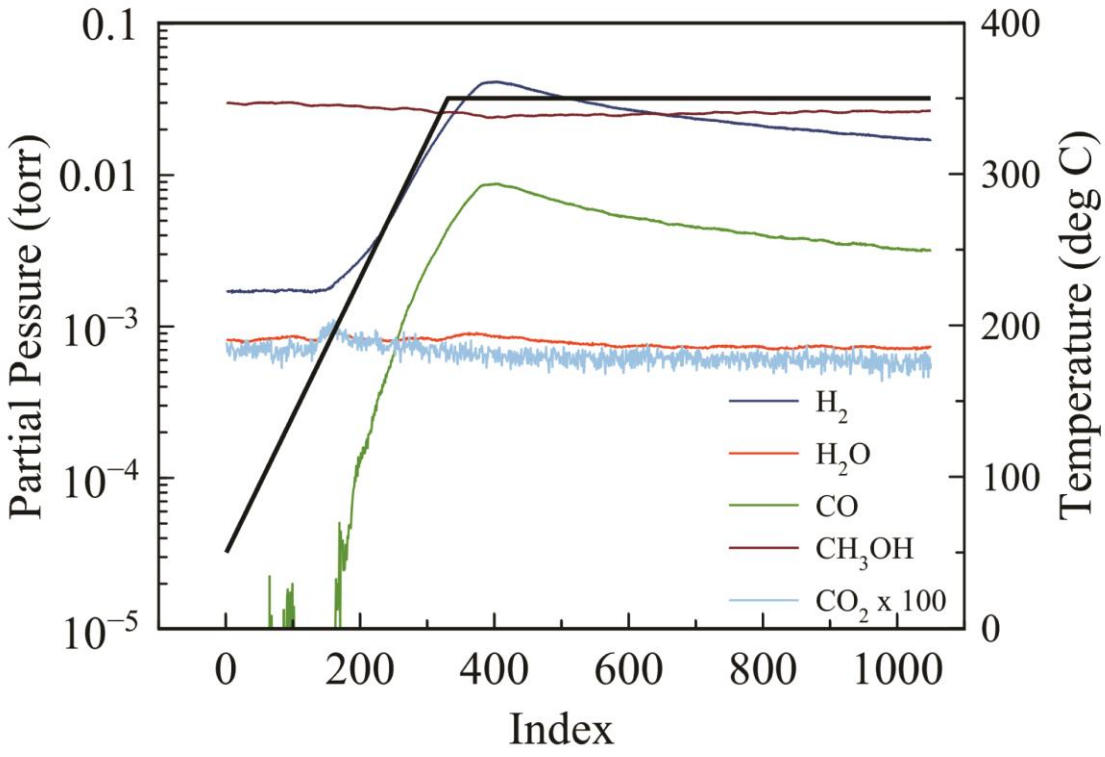

Figure 11: TPRS results for the methanol decomposition reaction run on the smallest (0% Pd(IV)) Pd catalysts.

A plot of the product and reactant traces for methanol decomposition on the smallest Pd nanoparticles is shown in Figure 11. Other samples tested showed a similar profile. Based on the results, the expected increase in conversion with temperature is observed. However, additional information can be gleaned. As the production of CO begins, a small peak in the CO_2 produced appears, along with a corresponding decrease in

the CO. However, as the reaction rate increases, the production of CO continues to increase, the production of CO_2 returns to its baseline value, indicating that the observed reaction is no longer occurring. This is indicative of a reaction occurring that converts CO to CO_2. As no new species were observed in the mass spectrometry data, it was concluded that a CO-disproportionation reaction was taking place, causing carbon to deposit on the surface of the Pd catalyst. Further, the amount of H_2 and CO produced increased with particle size, unlike in the case of MDR which showed the opposite trend. The presence of the reverse water-gas shift reaction can be seen in the slight increase in the water trace. These three pieces of information yield the reaction network presented in Figure 12.

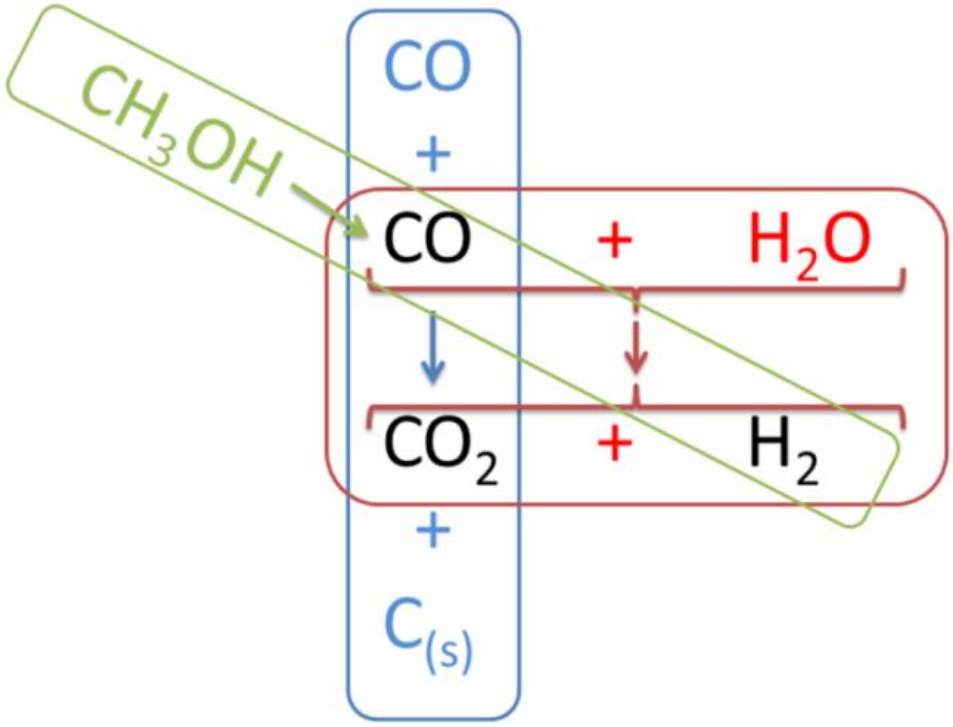

Figure 12: Reaction network as determined through TPRS studies. The methanol decomposition reaction is shown in green, the CO-disproportionation reaction in blue, and the reverse water-gas shift reaction in red. Common elements are in black.

The post-reaction TPO results show that the coking rate as a function of the Pd nanoparticle size goes through a maximum, as illustrated in Table 2. The amount of coking is directly proportional to the integrated area of the TPO carbon dioxide trace. As particle size increases, the selectivity to coking decreases, plateauing above a threshold size. This decrease follows from the decrease in the dispersion and the number of active sites. The reaction rate and methanol conversion follow opposite trends, increasing with size until a plateau is reached at a particle diameter of approximately 12nm.

Table 2: Change in Coking Rate with Particle Size

Sample	**Average Diameter (nm)**	**Coking Rate (micromol C/g cat/sec)**	**Surface Carbon pre-reaction (g/g-cat/hr)**	**Surface Carbon post-reaction (g/g-cat/hr)**
0% Pd(IV)	4.29	17.70	0.18	0.70
20% Pd(IV)	5.60	17.86	0.22	0.91
40% Pd(IV)	6.26	20.14	0.17	1.05
60% Pd(IV)	11.41	24.42	0.19	0.87
80% Pd(IV)	9.89	21.13	0.28	0.77
100% Pd(IV)	16.27	16.29	0.18	0.76

3.4. Conclusions

Pd nanoparticles of well-defined sizes were successfully fabricated using the one-pot polyol synthesis method with varying molar ratios of Pd(II) to Pd(IV) precursor and characterized with XRD, and TEM. The fabricated particles were then supported on silica and their catalytic properties were investigated using temperature programmed reaction techniques.

The size of the Pd nanoparticles was determined kinetically, as the two precursors used reduce at different rates in solution. As a result, the number of nucleation sites could be controlled, yielding nanoparticles of well-defined size. Based on the La Mer model, as

discussed in section 1.2.1, the different rates of reduction of the respective precursors resulted in a change in the concentration profile with time that caused a longer period of supersaturation, and thus more nucleation sites, with higher molar ratio of Pd(II) precursor.

XRD results confirmed the presence of metallic nanoparticles, with no formation of oxide or hydride phases. The particle size was calculated using the Scherrer equation, and found to be the same as the size measured in TEM to within one standard deviation. Further, the size of the nanoparticles fabricated was found through TEM imaging to correspond to the molar ratio of the precursors used, with a higher percentage of Pd(IV) precursor yielding larger particles. TPR and TPO runs confirmed the formation of little to no surface oxide or hydride phases during synthesis. Temperature programmed reaction results showed that the steady state generation of hydrogen increased with increasing surface area. This indicates that the methanol decomposition reaction is structure sensitive on Pd catalyst. The observed TOF both at peak and steady state increases roughly linearly with nanoparticle size. In contrast, the selectivity to coking decreases with size.

Chapter 4: Synthesis and Characterization of Shape-Controlled Ni-Pd Nanoparticles

4.1. Experimental Details

Similar to the polyol synthesis described in section 3.1.1 for the monometallic Pd particles, this synthesis uses the Ni(II) precursor nickel acetylacetonate (Formula: $C_{10}H_{14}NiO_4$), and Pd(IV) precursor ammonium hexachloropalladate (Formula: $(NH_4)_2PdCl_6$), and trimethyl(tetradecyl)-ammonium bromide (TTAB, Formula: $C_{17}H_{38}N{\cdot}Br$).

An excess of PVP (m.w. 40,000) was added to the Pd precursors, and then everything was dissolved in 10 mL of pentanediol. The solution was heated under argon atmosphere to 220°C and held at temperature for 20 minutes, as shown in Figure 6. In a typical synthesis, the synthesis vessel was pre-washed using an *aqua regia* solution, then rinsed with DI water and dried. One part $Ni(acac)_2$ (0.0125 mmol) and three parts $(NH_4)_2PdCl_6$ (0.0375 mmol) with respect to the molar mass of metal, an excess of PVP (2.0 mmol), and a predetermined ratio of TTAB to metal precursors (15:1 (0.75 mmol), 30:1 (1.5 mmol), 50:1 (2.5 mmol)) were dissolved in 10 mL of 1,5-pentanediol.

The particles are then precipitated with an excess (80 mL) of acetone. The supernatant is then removed, and the particles are resuspended in ethanol and washed three times, alternating hexane and ethanol to remove excess PVP. After washing, the particles are resuspended in 20 mL of ethanol.

In order to determine the best synthesis conditions for the formation of particles that would enable the testing of the influence of particle shape on the catalytic activity, the synthesis was run at three different temperatures: 140ºC, 160ºC, and 180ºC. This was repeated using three different molar ratios (15:1, 30:1, and 50:1) of TTAB, relative to the molar amount of precursors used.

4.2. Characterisation Techniques

XRD and TEM analysis was performed after each synthesis batch was made in order to determine the crystal structure, nanoparticle sizes, and shape distributions under each set of conditions. Low and high resolution TEM images were taken on an FEI Morgagni 268D at 60 kV and 180 kx and an FEI G^2 at 200 kV at 1.05 Mx, respectively. XRD was run on a Philips PAN'alytical diffractometer with a Cu Kα x-ray source (having a wavelength of 1.5418 Å) using scan settings of 45 kV, 40 mA, and a scan speed of 0.01 °/sec. STEM-EDX was performed on the FEI G^2 TEM in STEM mode at an accelerating voltage of 200 kV and a beam diameter of 2-3 nm. Both Ni and Pd were tracked during line scans.

The particles synthesized were subsequently supported on silica at 2 %wt. TPRS was run on two batches of the synthesized nanoparticles to demonstrate the effect of synthesis conditions on catalytic activity. The nanoparticles synthesized are active in methanol decomposition and ethylene hydrogenation.

4.3. Results and Discussion

TEM imaging (FEI Morgagni 268D; Figure 14 and Figure 15) reveals that the cubic nanoparticles synthesized have an average edge length of between 9 - 11 nm, as determined by measuring 100 nanoparticles and averaging the measured side lengths. These values are denoted in Table 3.

Table 3: Bimetallic NiPd Nanocube Synthesis Characteristics

Reduction Temperature (°C)	TTAB:precursor (mol:mol)	Average cube side length (nm)
140	30:1	9.7 ± 1.4
160	30:1	10.7 ± 1.2
180	30:1	10.7 ± 1.1
160	15:1	9.7 ± 1.3
160	30:1	10.7 ± 1.2
160	50:1	9.9 ± 0.9

The nanocube side length does not change by more than one standard deviation as the reduction temperature is changed, or the concentration of bromide ions is increased. This result suggests that the size of the nanocubes formed is a function of the amount of precursor used in the synthesis, rather than the synthesis conditions. The selectivity to nanocubes and nanorods is a strong function of these parameters, however, as shown in Figure and Figure . The portion of the sample comprised of nanocubes and nanorods is greater than 85% when a reduction temperature of 160°C and a TTAB-to-metal precursor ratio of 30:1 are used. Other combinations of synthesis conditions result in a lower selectivity. High resolution TEM imaging was done of a cube and a rod from this synthesis, as shown in Figure 13. Measurement of the interplanar distances based on these images was done by taking the average spacing over ten atomic planes.

Analysis of the synthesized nanoparticles using STEM-EDX (run on an FEI G^2 TEM, in STEM mode) demonstrates that the metal atoms are homogeneously distributed throughout the bulk of the nanoparticle. A line scan was run across both a cube and a pair of rods, as shown in Figure 16 and Figure 17, respectively.

Similar concentration profiles were observed for both metals, indicating that there was no segregation of Ni and Pd atoms into separate phases within the nanoparticles and confirming that the synthesis method used resulted in the production of Pd-rich nanoparticles, as would be expected. Based on the relative peak intensities observed in the Pd and Ni concentrations, a nanoparticle composition of approximately 28% Ni / 72% Pd is predicted, in good agreement with the precursor ratios used during synthesis.

XRD was run to determine the effect of shape control on the crystal structure of the synthesized nanoparticles, as well as to investigate the phase purity of the nanoparticle populations present in the samples synthesized. All synthesized samples were found to have the expected FCC crystal structure, regardless of reduction

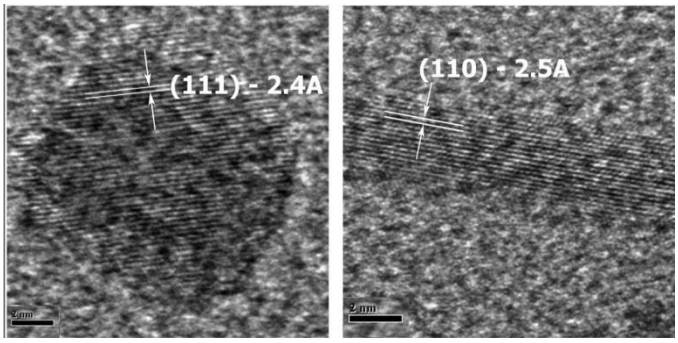

Figure 13: (left) HRTEM of a nanocube synthesized at a reduction temperature of 160°C, with a TTAB molar ratio of 30:1. (right) HRTEM of a nanorods synthesized under the same reaction conditions. Scale bars represent 2 nm, magnification used is 1.05 Mx, and the acceleration voltage used was 200kV.

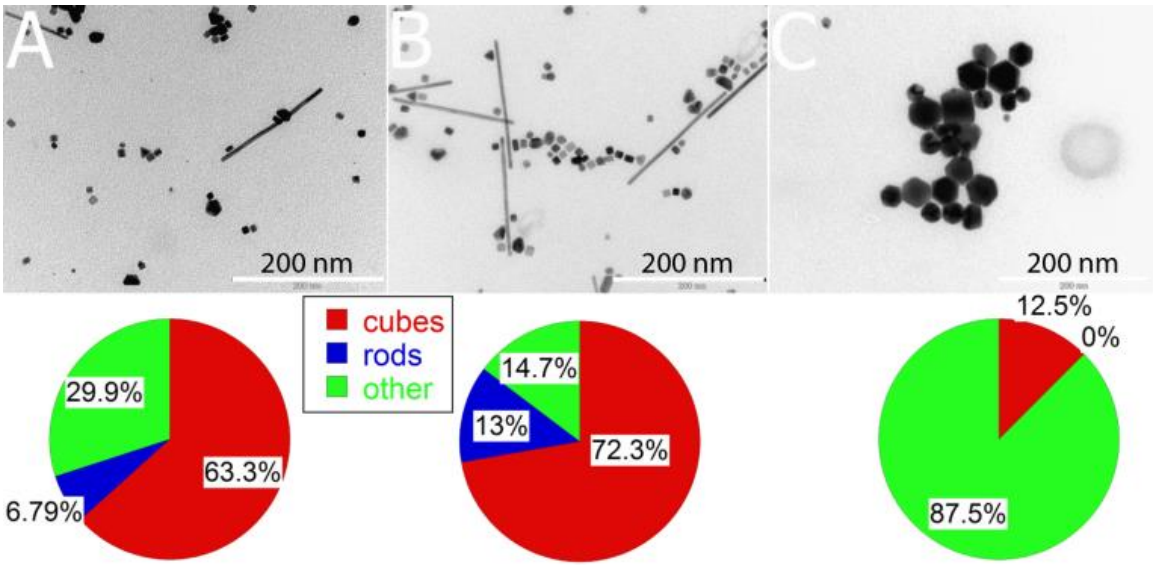

Figure 14: Influence of molar ratio of bromide ion to metal atom on shape distribution in NiPd alloy nanoparticles (A: 15:1, B: 30:1, and C: 50:1) at a reduction temperature of 160°C. Scale bars represent 200 nm.

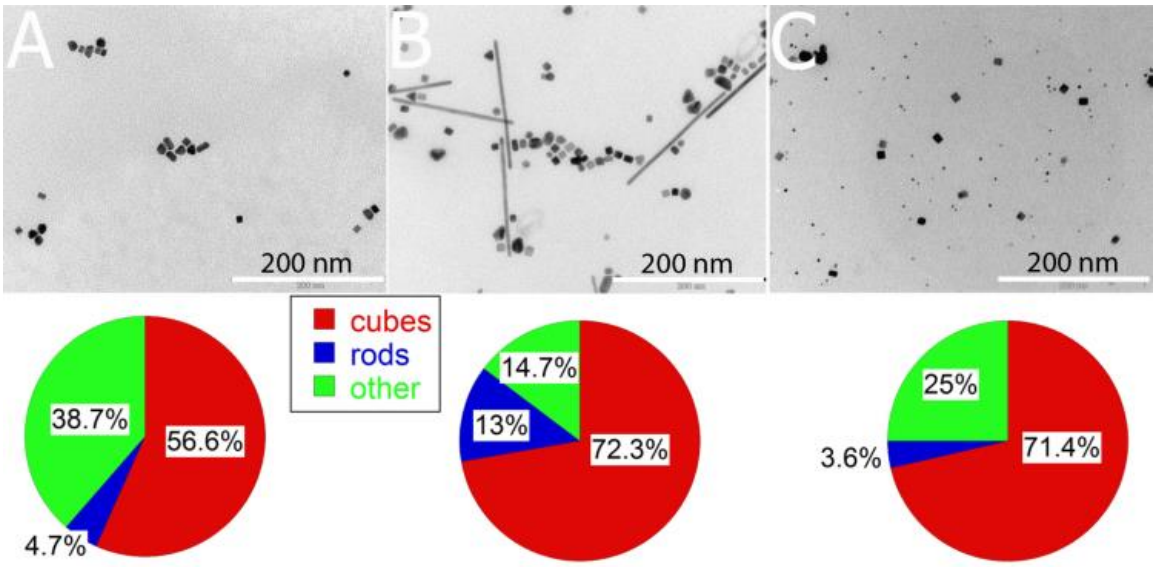

Figure 15: Influence of reduction temperature on shape distribution in NiPd alloy nanoparticles (A: 140°C, B: 160°C, and C: 180°C) with a TTAB:precursor molar ratio of 30:1. Scale bars represent 200 nm.

temperature or bromide ion concentration. If Vegard's rule is assumed to be valid, an alloy composed of 25% Ni / 75% Pd should have a diffraction line at approximately 41.1 degrees 2θ, when using a Cu Kα X-ray source. This diffraction line is not observed in the synthesized samples, however, appearing at 40.7° 2θ instead. This shift in the position of the diffraction line is indicative of either lattice strain within the nanoparticles as a result of the differences in atomic radius of the two component metals, or a shift in composition relative to the proportions of the metal precursors used in the synthesis.

If it is assumed that the crystal lattice of the synthesized nanoparticles is not under strain, the composition as calculated using Vegard's rule ranges from 13-17% Ni for the

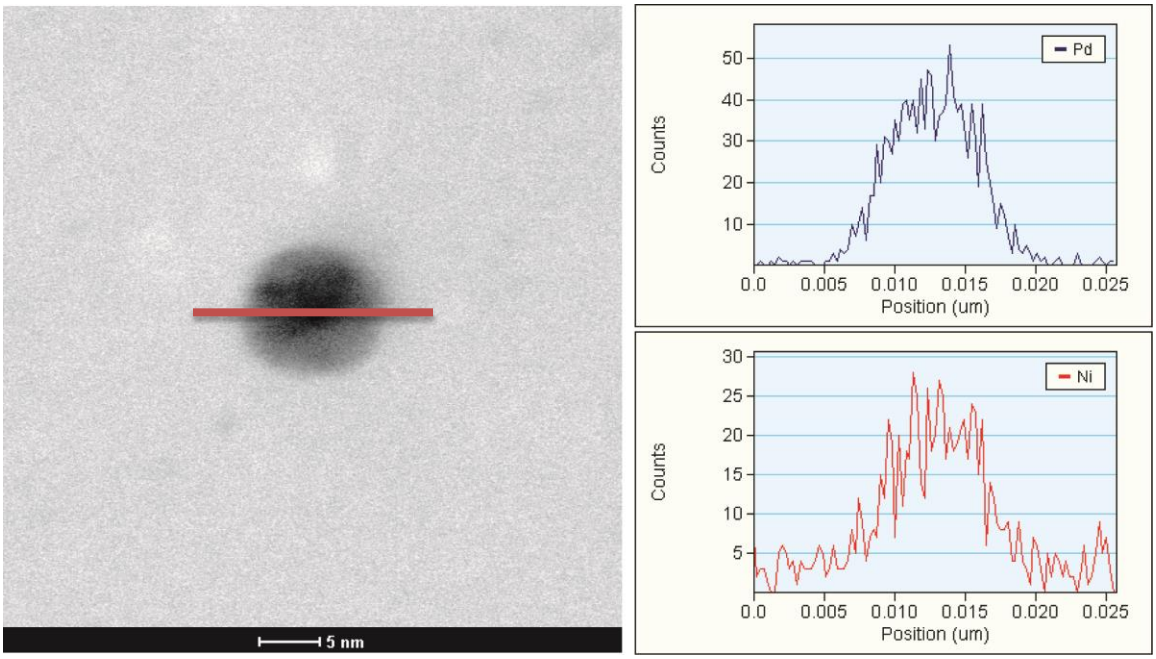

Figure 16: (left) The bright field STEM image of particles in the sample with the most cubes. The line scan was run along the red line. (top right) EDX line scan of the concentration of Ni at different points along the line scan. (bottom right) EDX line scan of the concentration of Pd at different points in the nanocube.

synthesized samples. The discrepancy between this value and the results obtained through STEM-EDX indicates that the no-strain assumption is not valid. Conversely, assuming that the composition of the nanoparticles is 25% Ni / 75% Pd, the calculated lattice strain for the samples ranges from 1-2%. The symmetry of the diffraction peaks was unaffected, signifying that the nanoparticles formed do not contain a high number of lattice defects, and that the crystal lattice is primarily undergoing uniform strain.

A second FCC phase is observed in all samples synthesized at a temperature of more than 140°C. This phase is present as a result of the formation of Pd-rich nanoparticles, as indicated by the close match with the reference Pd (111) diffraction line at 40.1° 2θ (JCPDS 46-1043). Assuming that the Pd-rich nanoparticles are not under strain, the calculated composition, using Vegard's rule is >98% Pd, suggesting that, once

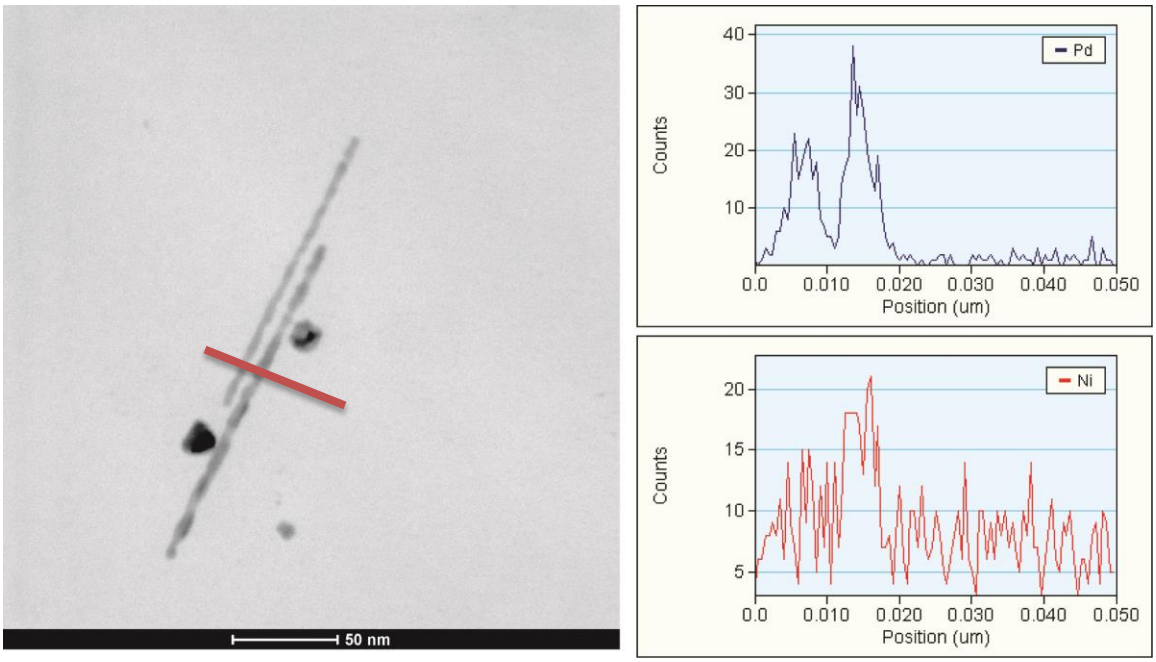

Figure 17: (left) The bright field STEM image of particles in the sample with the most cubes and rods. The line scan was run along the red line. (top right) EDX line scan of the Ni concentration. (bottom right) EDX line scan of the Pd concentration.

lattice strain is accounted for, the Ni content of this phase is likely less than 1%. The presence of a Pd-rich population of nanoparticles indicates that the bimetallic nanoparticles are likely formed early in the synthesis, and that, as the Ni atoms in solution are depleted, nanoparticles primarily composed of Pd atoms begin forming. The possible formation of NiO is suggested by the remaining diffraction line observed at circa 36.6° 2θ. However, in the TEM images presented, the presence of an oxide surface layer would be difficult to distinguish as a result of the amorphous layer of capping polymer coating present in all samples. Further, the diffraction line observed near 36.6° 2θ does not match up with the literature value of 37.3° 2θ for the NiO (111) plane (JCPDS 4-835). Based on the observed peak position, a strain of 1.5-2% would be expected for any pure NiO formed. However, this does not address the reason for the expansion of the NiO lattice. Assuming that no strain is observed, this diffraction line would be attributed to a complex oxide composed of NiO where approximately 6% of Ni lattice sites are occupied by a Pd atom. Given that the no-strain assumption is likely not applicable to this peak, the composition is known to be less than the calculated 6%. The precise composition is difficult to determine, however. Therefore, though the exact composition is not known, the diffraction line at 36.6° 2θ is assigned to the (111) plane of the formed complex oxide. In some samples, a low intensity peak is seen at approximately 42.6° 2θ, which correlates to the (200) plane of the observed complex oxide phase. No higher index planes of the complex oxide are observed, indicating that the complex oxide is forming either as a population of nanoparticles with very small diameter, or as a thin surface layer on the bimetallic nanoparticles synthesized. The

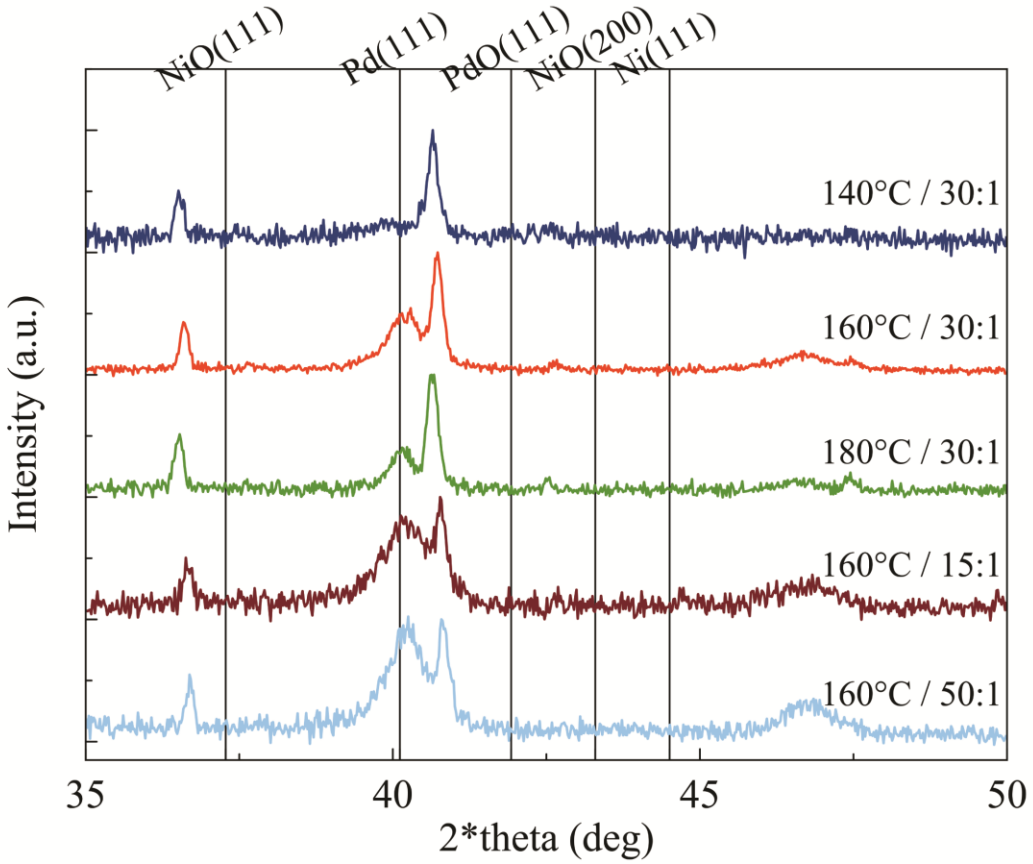

Figure 18: XRD profiles of all NiPd nanoparticle samples. Scans were done at ambient conditions using a Cu Kα x-ray source at 45 kV and 40 mA, with a scan speed of 0.01 °/sec. Low index peaks of reference materials are shown for comparison.

formation of a population of very small nanoparticles -- with a diameter of about 2-3 nm -- a significant amount of peak broadening would be expected in the recorded diffractograms. This is not the case, though, indicating that the diffraction lines detected are most likely due to oxidation of the nanoparticles' surface.

HRTEM images of the sample having the highest selectivity toward the formation of nanocubes and nanorods -- synthesized using a reduction temperature of 160°C and a TTAB-to-metal precursor molar ratio of 30:1 -- the interplanar distances of the (111) and (110) planes was measured by averaging the interplanar distance over 10 atomic planes.

This yielded interplanar distances of 2.4 and 2.5 Å for the (111) and (110) interplanar spacings, respectively. These interplanar distances correspond to unit cell side lengths of 0.42 and 0.43 nm, respectively. Unit cells of this size would generate diffraction lines at ~36 and 37° for the x-ray source used in these experiments (Cu Kα). These values closely agree with the diffraction line observed at 36.6° 2θ, demonstrating that the observed oxide phase is a thin surface layer, rather than a separate population of small nanoparticles.

4.4. Conclusions

A modified polyol synthesis with shape control has been demonstrated for bimetallic Pd-based alloy nanoparticle catalyst. The cube and rod shaped nanoparticles were found to comprise >85% of the synthesized nanoparticles. Further, the synthesized nanoparticles show bimetallic character, and homogeneous composition over the volume of a nanoparticle.

Based on the results of x-ray diffractograms collected, the concentration of bromide ions used to stabilize the (100) and (110) facets of the synthesized nanoparticles also affects the relative populations of bimetallic and Pd-rich nanoparticles that are formed. A higher concentration of bromide ions results in a larger population of Pd-rich nanoparticles, based on the relative intensities of the Pd and bimetallic peaks observed in XRD. The formation of a thin surface oxide layer was also observed. Control of the reduction temperature was also shown to have an effect on the shape distribution of the synthesized nanoparticles, though not to the same degree as the bromide ion concentration.

Based on analysis of the shape distributions observed through TEM imaging, it was concluded that the best synthesis conditions to use to achieve a high selectivity to nanocube and nanorods formation is a reduction temperature of 160°C and a bromide-to-precursor molar ratio of 30:1. Conversely, XRD indicates that to avoid the formation of Pd-rich nanoparticles, a reduction temperature of 140°C is better, as no Pd-rich phase is observed. This suggests that the relative difference in the reduction rates of the two precursors used is small enough at the lower temperature to allow for the formation of primarily bimetallic nanoparticles.

Chapter 5: Effect of Shape and Composition on SPR in Ag and Pd Nanoparticles

The metal enhanced luminescence properties of silver have been extensively studied[33, 111-116] as a result of its narrow and intense SPR peaks. Further, gold has been shown to have size-dependent properties[117-119], while copper has been shown to enhance luminescence[120]. Both luminescence enhancement and quenching have been successfully used for a variety of applications, including enhanced wavelength-ratiometric sensing[23], amplified assay detection[24, 25], optical detection of DNA hybridization[25, 26], and high throughput immunoassays[27], among others.

Similarly, because bimetallic nanoparticles have excellent optical, electronic, and catalytic properties relative to their bulk counterparts and have wide ranging applications in such areas as catalysis, sensing, and SERS, they have been the focus of much attention in the areas of novel synthetic methods development and nanoscale characterization[2, 6, 19, 29, 42, 56, 58, 69, 74-76, 80, 81, 84, 87, 90, 102, 103, 121-141]. Ag@Pd core-shell nanoparticles, where the notation describes a core@shell configuration, have been synthesized with high yield using ultra high vacuum techniques[121], as well as lower-cost methods such as microwave-assisted reduction[122] or a polyol synthesis[123].

It has been shown in the literature that Au can be used in the design and implementation of oligonucleotide sensors based on the quenching effect that occurs when a fluorophore is in close proximity to a gold nanoparticle[142, 143]. The principle of this sensor is that the donor fluorescence is quenched so long as a loop-like single-

stranded DNA (ssDNA), remains in its closed position. In this type of sensor, known as a molecular beacon type sensor, the fluorophore is bound to a strand of ssDNA which is functionalized to the surface of a noble metal nanoparticle with a thiol group. In the closed position, the ssDNA loop brings the fluorophore close to the surface of the nanoparticle, resulting in quenching of the fluorescence. The loop of ssDNA used is complementary to an ssDNA target that the sensor is meant to detect. When the complementary ssDNA strand comes into proximity to the sensor, the loop of ssDNA shifts into its open position, and the quenching effect is lessened.

The aim of this study is to investigate the potential applications of physical mixtures of Ag and Pd nanoparticles in a similar type of sensing application. The effects of physical mixtures of differing combinations of the coinage metals have not been investigated in detail in the literature. In this work, we address the effect of shape control on the optical response of physical mixtures of Ag and Pd nanoparticles with well-defined shape and size.

5.1. Experimental Details

In this study, Ag nanocubes and Pd nanoboxes with a range of shell thicknesses were synthesized using a polyol process. The Ag nanocubes were synthesized as described by Tao et al[6]. The Pd nanoboxes were subsequently synthesized using a seed mediated polyol synthesis in which the Ag nanocubes acted as a sacrificial template for the Pd nanoboxes. Silver nitrate (>99%), and copper(II) chloride dihydrate (>99.999%), were obtained from Sigma-Aldrich Co., MO, and used as received. Polyvinylpyrrolidone

(PVP, 58 000 molecular weight) was purchased from Alfa Aesar. All solvents used were analytical grade and used without further purification.

In a typical Ag nanocube synthesis, the synthesis vessel was pre-washed using an *aqua regia* solution, then rinsed with DI water and dried. 500 mg and 86 μg of copper chloride and silver nitrate were dissolved together in 12.5 mL 1,5-pentanediol. 250 mg of PVP were separately dissolved in an additional 12.5 mL 1,5-pentanediol. Subsequently, 20 mL of 1,5-pentanediol were heated to a temperature of 180°C in a three necked flask under Argon atmosphere and stirring. After 10 minutes, the two precursor solutions were injected into the hot reaction flask at different rates. Every 1 minute, 0.5 mL of AgNO3 solution was injected, and every 0.5 min, 0.25 mL of PVP solution was injected. This was continued until the solution became opaque (after approximately 6 minutes), indicating the formation of nanocubes.

The Pd nanoboxes were synthesized by means of an adapted seed mediated polyol synthesis. Nanoboxes of three different wall thicknesses (5, 8, and 10 nm) were synthesized for characterization. First, 1 mmol PVP (based on the monomer unit) and the appropriate amount of Pd precursor (0.005, 0.1125, and 0.025 mmol, respectively) were added to a three-necked flask pre-cleaned as described above. The PVP and Pd precursor were dissolved in 9 mL 1,5-pentanediol and bubbled with argon for 10 minutes. 1 mL of as-synthesized Ag nanocubes were added to the three-necked flask, and allowed to mix evenly under stirring. The suspension was then heated to 160°C in a pre-heated oil bath and held at temperature for 20 minutes, maintaining the Ar atmosphere. The nanoparticle suspension was allowed to cool in the oil bath, then precipitated with acetone.

Precipitated samples were then washed three times in ethanol and hexanes prior to characterization. After completion of the synthesis, the precipitated suspension obtained was centrifuged for 5 minutes at 6500 RPM, and the supernatant acetone was discarded. The precipitate was resuspended in 1 mL of ethanol. After mixing was ensured through sonication, 14 mL of hexanes were added to the flask and the resulting suspension was centrifuged again. This process was repeated two more times. The resulting precipitate was resuspended in 10mL ethanol for characterization.

An Ag sample without shape control was synthesized as well, for comparison. The sample was prepared using the same procedure as detailed for the Ag nanocubes, with the only change being the number of injections of Ag precursor solution and solvated PVP. Instead of stopping after 6 minutes, the process was continued until the 9 minute mark.

5.2. Characterisation Techniques

TEM images were taken on an FEI Morgagni 268D. Images were taken at 60 kV and 71 kx. TEM samples were prepared by dispersing a drop of nanoparticle solution (diluted in ethanol by a factor of 10) on a carbon formvar film supported by 200 mesh copper grids. XRD was performed using a Philips PAN'alytical diffractometer with settings of 45 kV, 40 mA, and a scan speed of 0.01 °/sec after the nanoparticle suspension had been deposited on a cleaned glass slide. A Cu Kα x-ray source with a wavelength of 1.5418 Å was used. EDS analysis was done on a Hitachi SU-70 SEM at an acceleration voltage of 6 kV and a magnification of 300 kx. A UV-vis spectrometer (Perkin Elmer,

Lambda 35) was used to measure the absorption spectra of the synthesized nanoparticles in suspension with neat ethanol used as a background.

5.3. Results and Discussion

Based on TEM results, the Ag nanocubes synthesized were found to have a side length of 57.5 ± 6.5 nm. This was found by counting and measuring 200 nanocubes and calculating the mean and standard deviation of the measured side lengths.

The sample exhibited primarily cubic morphology, with a small population of polyhedral and rod-shaped nanoparticles. The sample synthesized under conditions that favored the formation of polyhedra showed almost no cubes forming, and a slightly higher population of rod-shaped nanoparticles, as shown in Table 4.

Table 4: Ag Nanoparticle Shape Distributions.

Sample:	Cubes (%)	Rods (%)	Triangles (%)	Polyhedra (%)
Ag Nanocubes	79.70	1.16	5.99	13.15
Ag Polyhedra	1.25	6.06	6.37	86.31

After the Pd nanoboxes were synthesized, the side lengths observed increased, proportional to the wall thickness, as shown in Figure 20D, and the shape distributions observed in the Ag nanocubes were maintained. The observed change in contrast between the Pd nanoboxes formed and the Ag cores as observed in TEM imaging indicates that the cubes are not core-shell particles, as was expected. Normally Ag and Pd would not show any change in z-contrast in TEM, due to the similarities of their respective atomic masses, and so we concluded that during the core-shell synthesis the Ag core of the

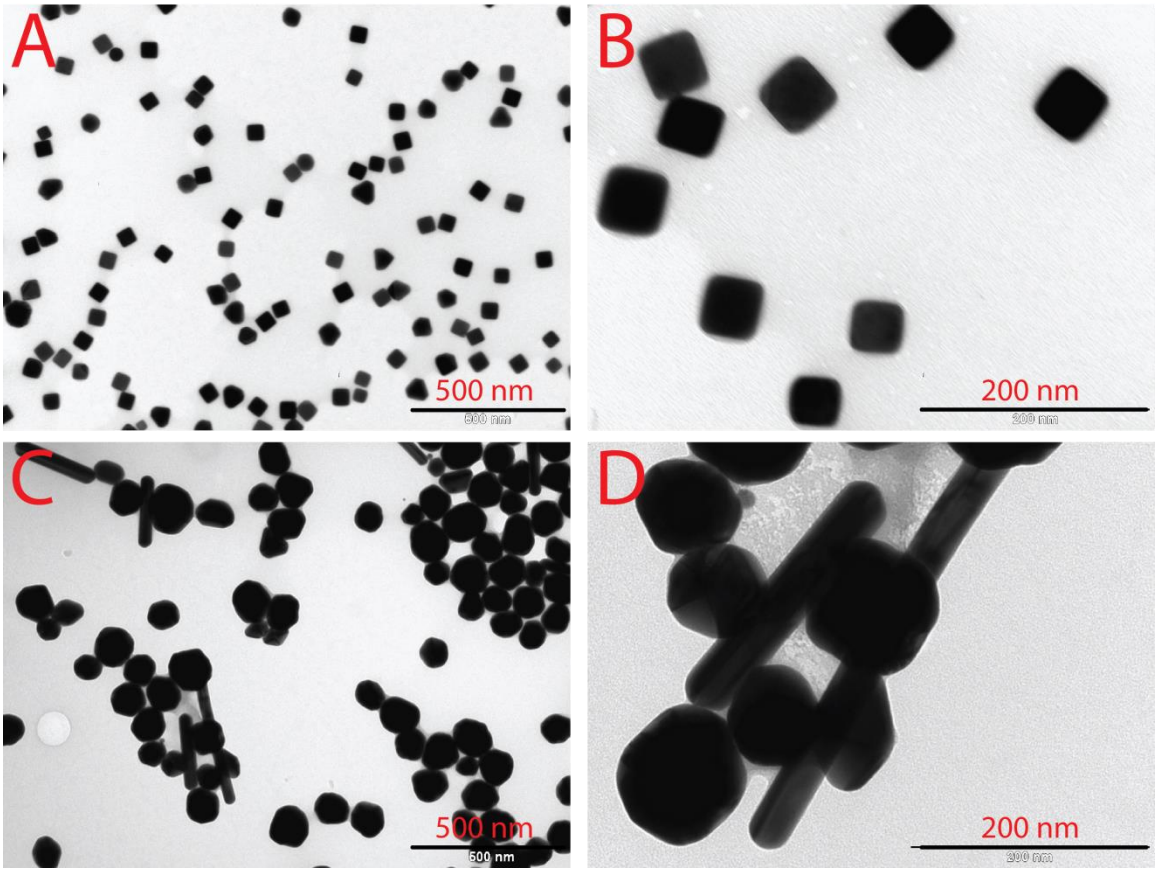

Figure 19: TEM images of Ag nanocubes and polyhedra taken at an acceleration voltage of 60 kV and a magnification of (A,C) 44kx, and (B,D) 180kx.

nanocubes was sacrificed, yielding hollow Pd cubes with small amounts of silver substituted into the Pd lattice as a result of the Ag atoms diffusing out through the Pd layer as it formed. This can be observed in the XRD peaks yielded by the hollow Pd samples synthesized, as shown in Figure 21. In TEM images of the as-synthesized Pd nanoboxes a large population of small spherical nanoparticles with a diameter of 10-15 nm can be perceived. These represent the re-nucleation of the ionized Ag atoms due to re-reduction by the polyol solvent as the synthesis vessel cooled. In order to isolate the effects of the Pd nanoboxes in UV-Vis measurements, 1 mL of each of the three

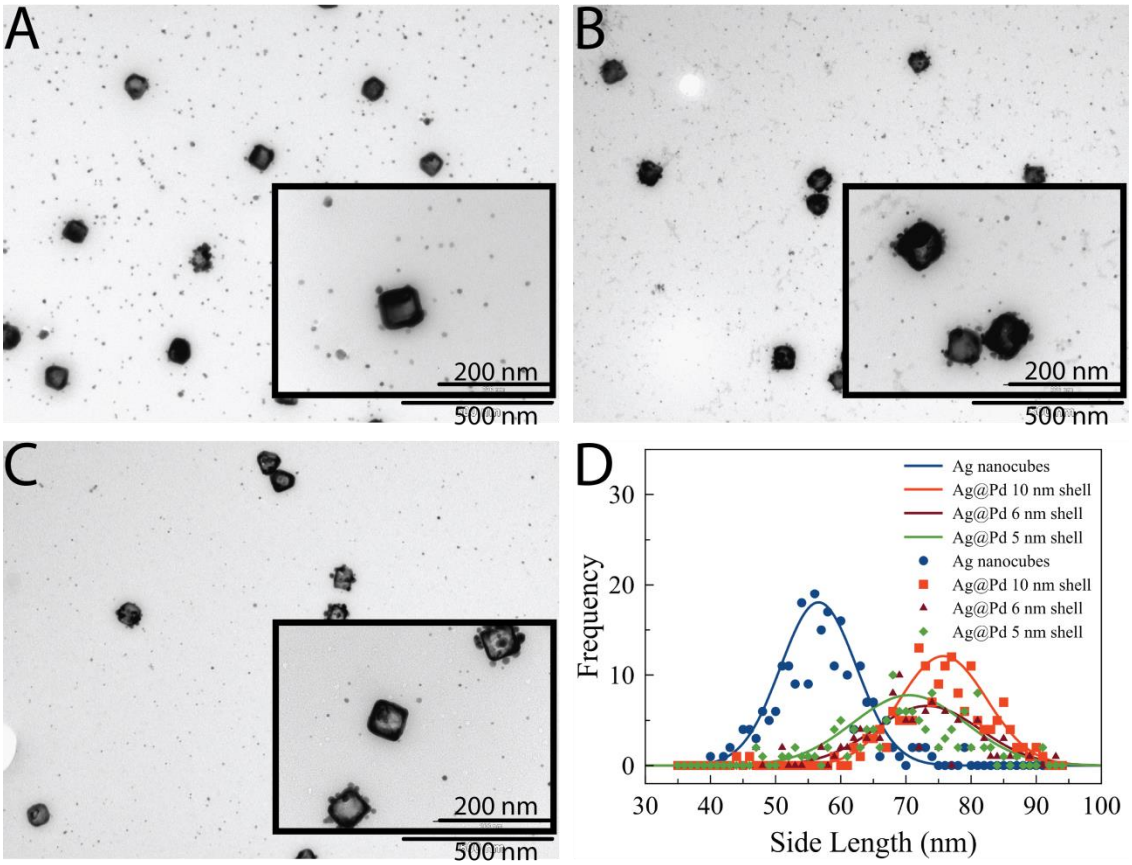

Figure 20: TEM images of Pd nanoboxes with (A) 10 nm Pd shell, (B) 6 nm Pd shell, and (C) 5 nm Pd shell. All images are taken at 60 kV and 71kx. The scale bar represents 500 nm. All insets are taken at 60 kV and 180kx. The scale bar represents 200 nm. (D) Plot of histogrammed nanocube side lengths.

synthesized Pd nanobox suspensions was centrifuged for 10 minutes at 1000RPM and room temperature to separate the nanoboxes from the small spherical Ag nanoparticles.

The collected XRD data shown was taken using the as-synthesized samples before centrifuge separation of the Pd nanoboxes. It was observed that the Ag nanocubes synthesized remain mostly in their metallic state, with only a small AgO(311) peak appearing at 65.3° 2θ, as presented in Figure 21. The AgO(111) peak cannot be resolved except through peak deconvolution, as it overlaps with the Ag(111) peak. Peak

deconvolution reveals that a small AgO(111) peak is present, while the bulk of the signal originates from the Ag nanocubes present in the sample, as shown in Figure 22. The remaining broad low-intensity peak is attributed to the formation of AgCu alloy nanoparticles during the synthesis procedure, as a result of the $CuCl_2$ used, as will be discussed further.

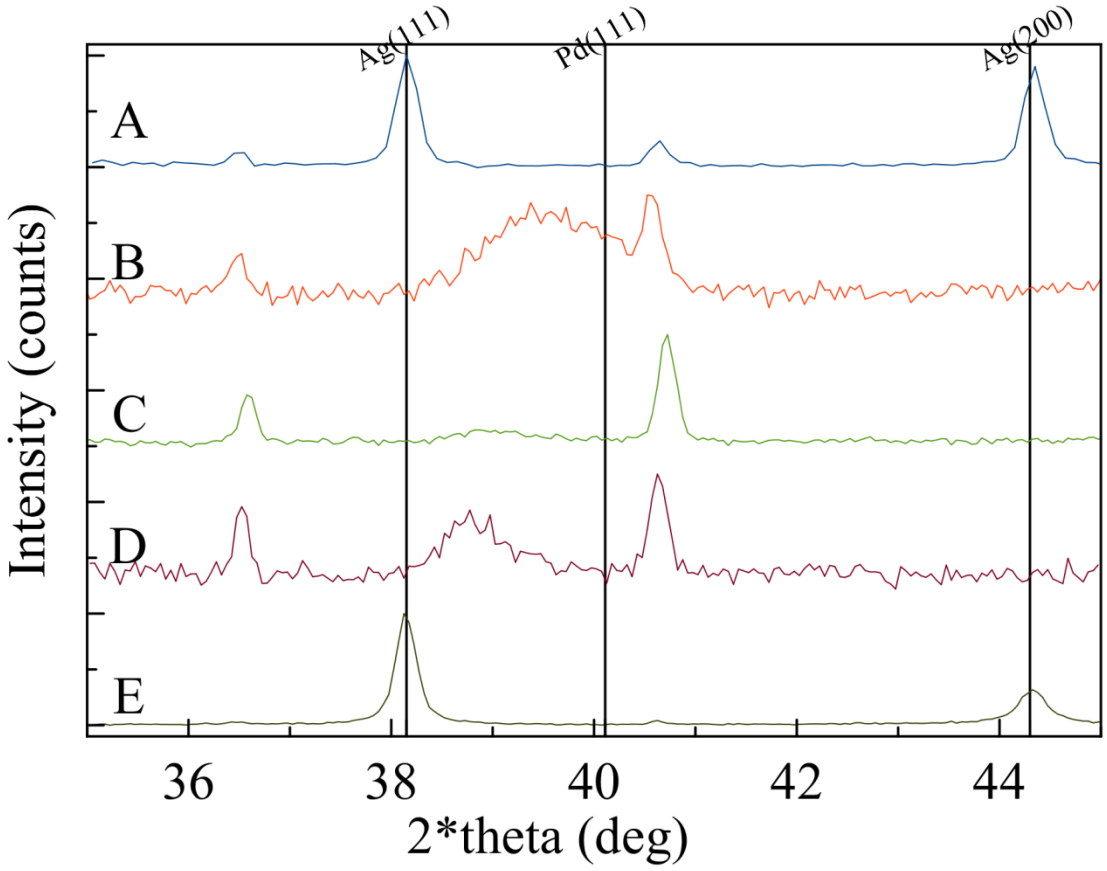

Figure 21: X-ray diffractograms of (A)Ag nanocubes, (E)Ag polyhedra, and Pd nanoboxes with (B)10 nm, (C) 6 nm, and (D) 5 nm wall thicknesses.

The relative peak intensities exhibited by the Ag nanocubes are also different from those of single crystalline silver. The relative intensities of the (111) and (200) peaks in Ag are listed as 100% and 42%, respectively, on JCPDS card 4-783. In the synthesized Ag nanocubes, the observed intensities were 100% and 95%. As the intensity

of the signal seen in XRD is directly proportional to the number of and size of the planes present in a sample with a given index, this change is ascribed to the higher proportion of (100) planes present in the nanocubes, relative to the lower energy prisms bounded by (111) facets that Ag would form under synthetic conditions not incorporating shape control.

The nanocubes synthesized also show minimal oxidation of the exposed (100) surfaces. The observed AgO peaks are of low intensity, indicating the formation of a very

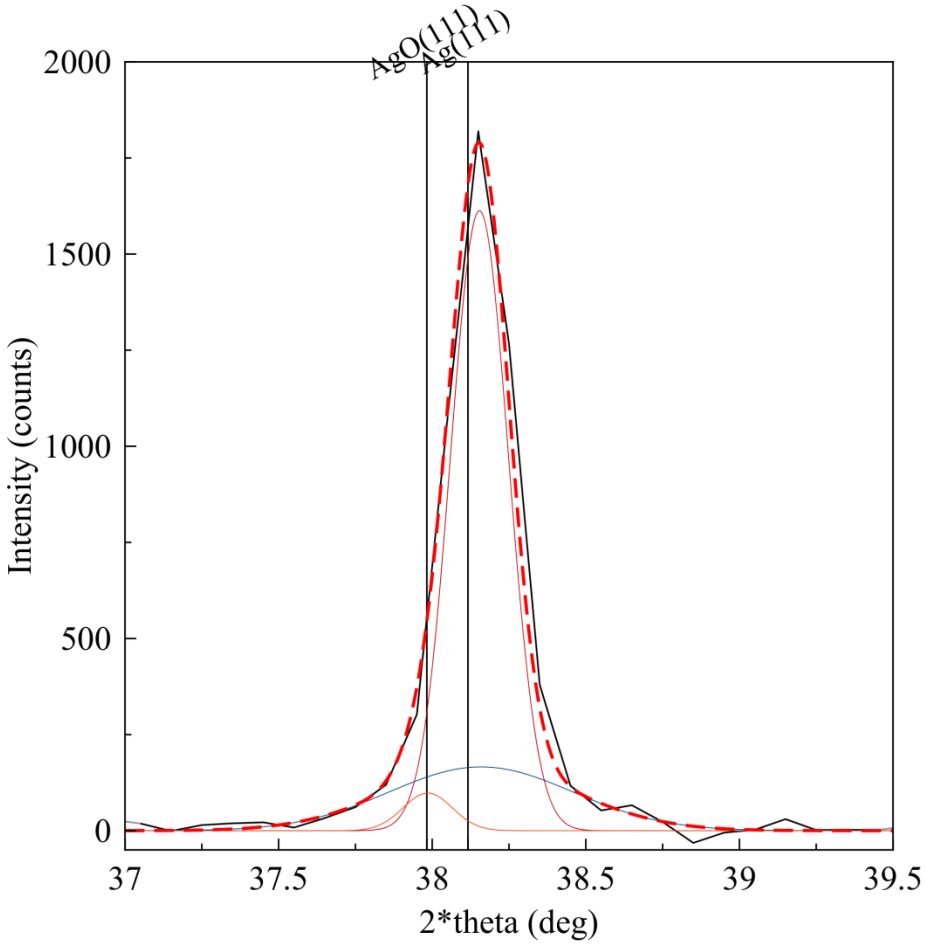

Figure 22: Deconvolution of Ag(111) and AgO(111) XRD peaks observed in Ag nanocubes.

thin surface oxide layer on the surface of an Ag nanocube, rather than the formation of a metal oxide nanoparticle.

As was briefly mentioned above, it can be demonstrated that the presence of the $CuCl_2$ precursor has a direct impact on the composition of the nanoparticles formed. While the chloride ions released into solution by the dissociation of the precursor act to form the Ag nanocubes observed, the Cu ions become reduced by the polyol solvent alongside the Ag ions, becoming substituted into the Ag lattice as it forms. Because the Ag ions are present in excess, relative to the Cu, only a small population of the Ag cubes synthesized contain Cu atoms within their lattices. Thus, the low intensity of the AgCu alloy peak relative to the Ag peaks is a direct result of the relative molar amounts of metal present in the polyol solution during the synthesis. Two peaks appear (at 36.5° and 40.6° 2θ, respectively) that can be attributed to the Cu atoms which become substituted into the Ag lattice. The lower angle peak at 36.5° is attributed to the surface oxide layer that forms on the AgCu alloy.

The peaks observed between 38.8° and 39.5° 2θ are AgPd alloy peaks which are likely a result of both the Pd nanoboxes and the small spherical nanoparticles present in the solution. The shift in the peak position from 39.5° 2θ to 38.8° 2θ occurs as a result of the relative molar amounts of Ag and Pd used in the core-shell synthesis. The higher the molar amount of Pd used in the synthesis, the more the peak is shifted in position toward the peak position of pure Pd (40.115° 2θ). The persistence of the AgCu alloy peaks in the Pd nanobox samples indicates that the difference in galvanic potential between the Ag and Cu atoms is enough to cause the AgCu nanocubes to maintain their stability during the templated synthesis, unlike the pure Ag nanocubes, whose Ag cores are leeched out

of the nanoboxes and into solution as a result of the electronegativity differences during the synthesis procedure. The AgCu peak maintains its intensity and shape, indicating that the size and crystallinity of the AgCu nanocubes are not measurably affected. The position of the peak is slightly shifted, however, suggesting that during the synthesis of the Pd nanoboxes some strain is induced in the AgCu alloy particles.

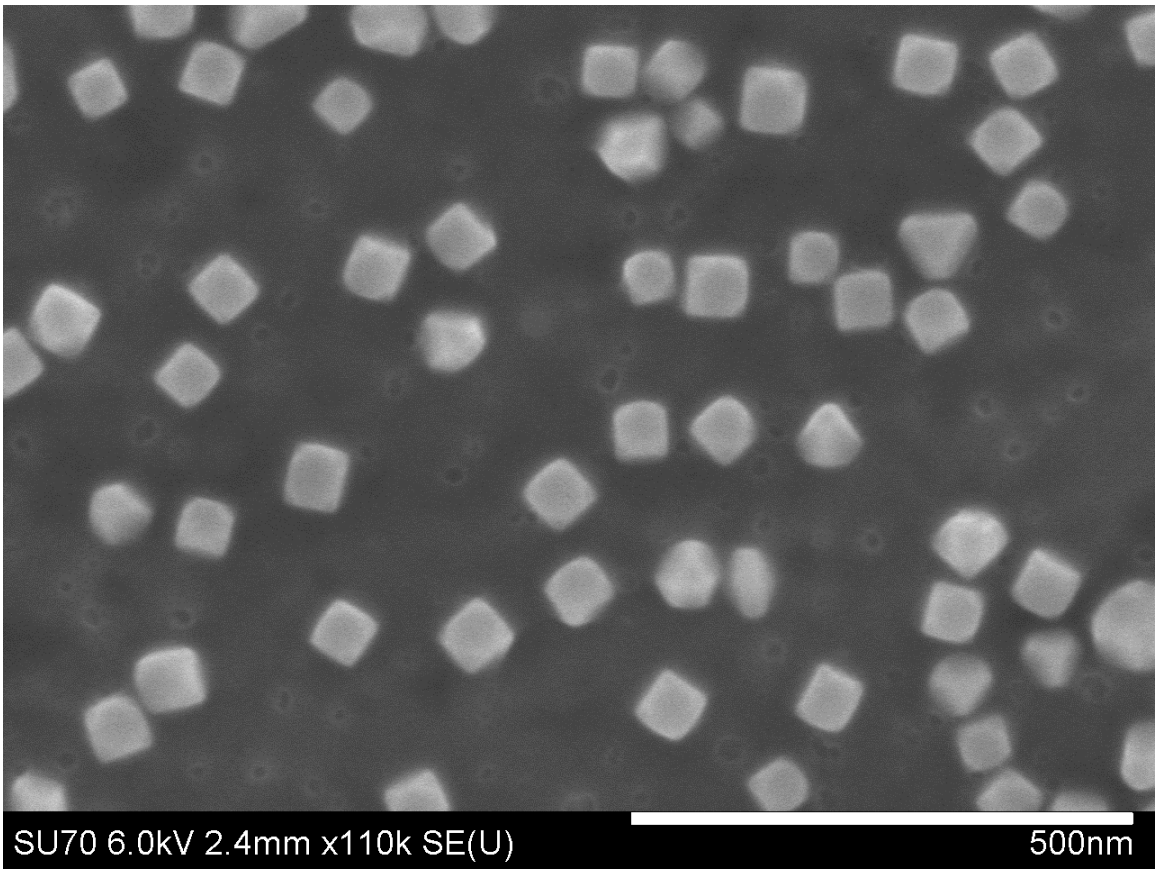

Figure 23: SEM image of Ag nanocubes synthesized.

SEM imaging confirms the presence of Ag cubes, as shown in Figure 23. EDS line scans were run, but did not yield quantifiable data, due to the algorithms used by the EDS software. Because the EDS software assumes a bulk sample, infinitely wide and thick relative to the electron beam excitation volume, the calculated values of the

respective metals present, as provided by the software are incorrect. Monte Carlo simulations used to model the excitation volume were done using the freeware program Casino 3.2 (http://www.gel.usherbrooke.ca/casino/What.html). Based on the results of the Monte Carlo simulations, as shown in Appendix 2, the acceleration voltage of 6 kV was chosen. A set of representative results is shown in Figure 24. Because the software calculates the composition of the sample based on the relative counts, the non-zero baseline measured for Cu makes this measurement technique unusable. It is likely that the nonzero baseline is being caused by the use of the Cu formvar grid during analysis being excited by part of the electron beam. At 6 kV the excitation volume of the electron beam is not entirely contained within the nanocube.

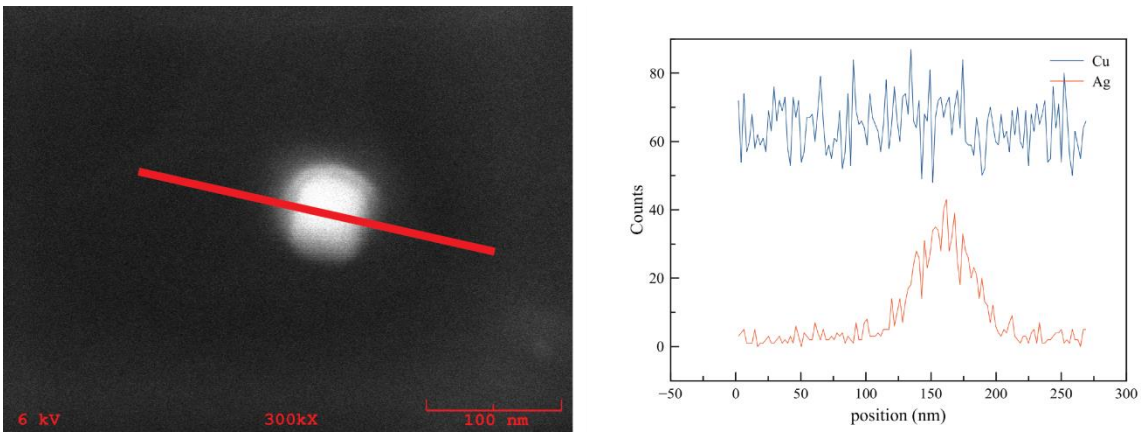

Figure 24: SEM image of an Ag nanocube and its corresponding EDS line scan. The image and scan were taken at an accelerating voltage of 6 kV and a magnification of 300 kx.

The changes in crystal structure correspond to the changes in absorbance observed in UV-Vis spectroscopy. As would be expected, given that the Ag core was used as a sacrificial template, the intense Ag absorption peak observed at a wavelength of

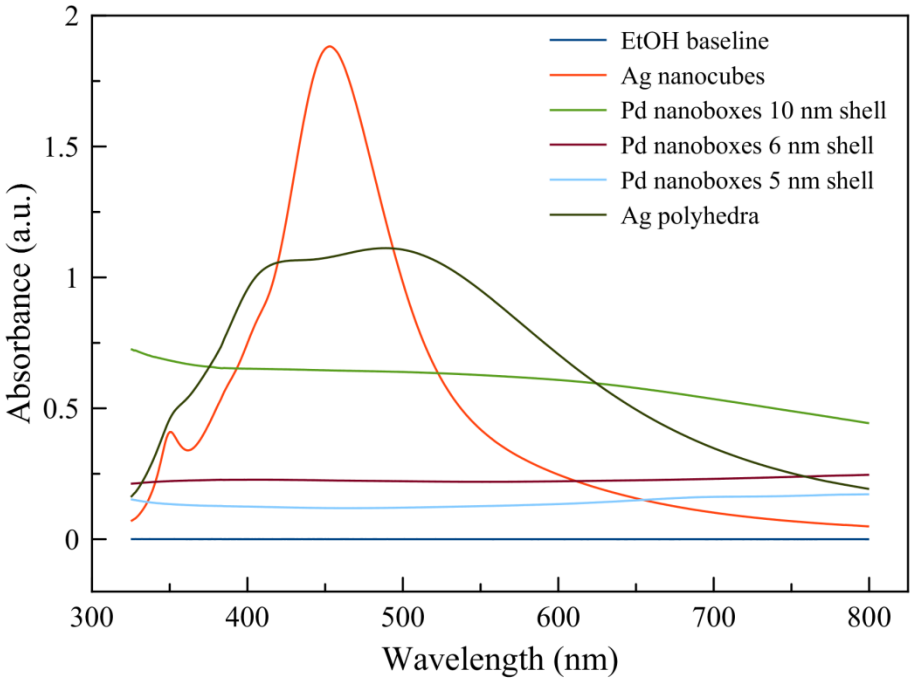

Figure 25: UV-Vis spectra of Ag nanocubes, polyhedra, and hollow Pd nanocubes.

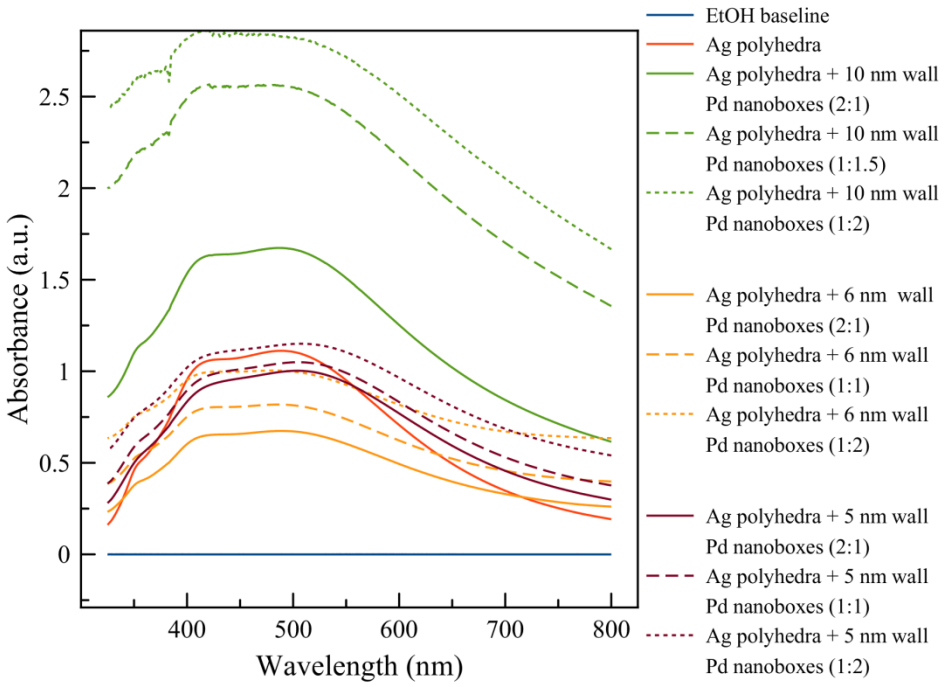

Figure 26: UV-Vis spectra of physical mixtures of Ag polyhedra and as-synthesized Pd nanoboxes. Ratios noted are volume ratios; respective Ag and Pd nanoparticle stock concentrations are kept the same, on a mL basis.

450 nm disappears, and is replaced by a low broad absorption throughout the visible spectrum as is characteristic of Pd[1].

The UV-Vis data presented in Figure 25 indicates that the synthesized Ag nanocubes absorb light throughout much of the visible portion of the spectrum with peaks at 450 nm and 350 nm, and is in good agreement with the behavior observed in the literature[6, 13]. A slight shoulder appearing at about 410 nm is indicative of the presence of other prisms in the synthesized sample. After the synthesis of the Pd nanoboxes, the absorbance peak at 450 nm disappears, and is replaced by a broad absorbance throughout the visible portion of the spectrum. In the case of the Ag polyhedra, a broad doublet peak appears that spans much of the visible range, rather than a single well-defined absorbance

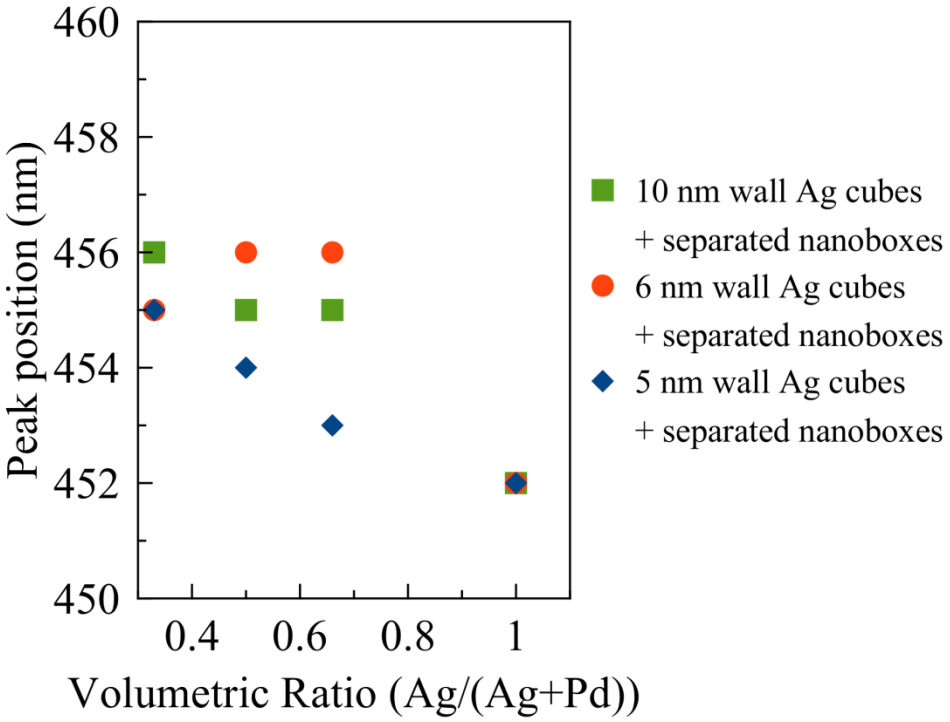

Figure 27: Variation in UV-Vis peak positions of physical mixtures of Ag polyhedra and fractionated Pd nanoboxes. Ratios noted are volume ratios; respective Ag and Pd nanoparticle stock concentrations are the same.

peak. Further, the changes in absorbance correlate with the shell thickness. The nanoboxes synthesized with thicker walls absorb more intensely than those with thinner shells as a result of the higher amount of Pd per mL of suspension, when calculated on a mass basis. The number of nanoparticles present per mL is kept the same for all Pd nanobox suspensions.

The Ag polyhedra did not show any significant peak shifting when combined with the Pd nanoboxes in a physical mixture, as shown in Figure 27. The ratios of the respective nanoparticle suspensions added to the cuvette are given on a volume basis, as

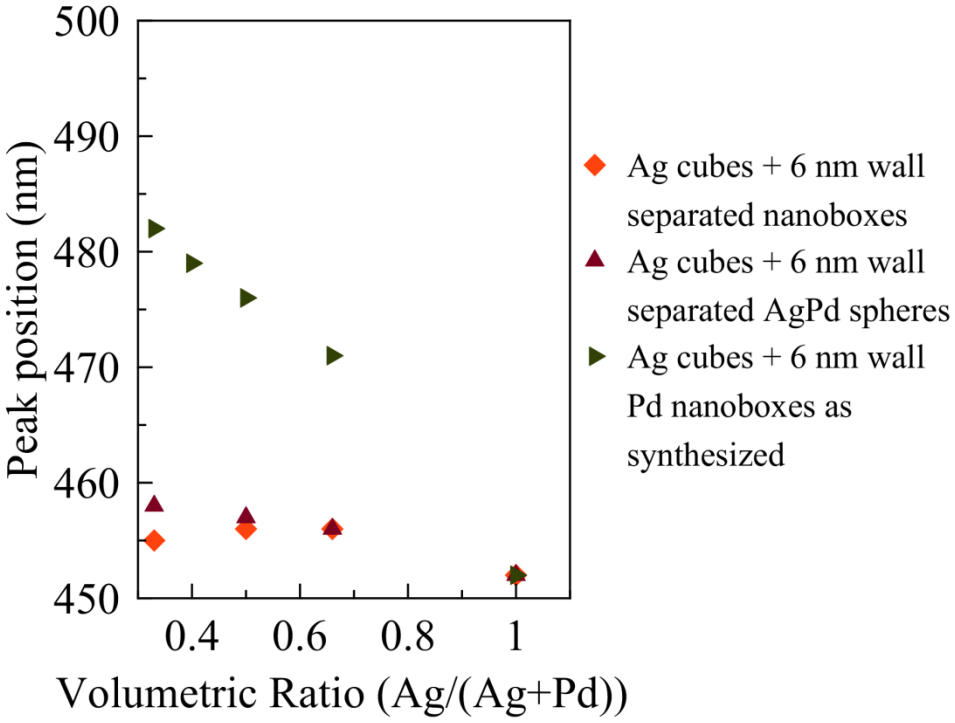

Figure 28: Variation in UV-Vis peak positions of physical mixtures of Ag cubes and fractionated 6 nm wall Pd nanoboxes. Respective Ag and Pd nanoparticle stock concentrations are the same.

the concentrations of nanoparticles per mL in the respective solutions was kept constant. Some damping of the observed peaks was seen, for the 5 nm and 6 nm wall Pd nanoboxes, in addition to the shift in the baseline absorbance.

The physical mixtures of Ag nanocubes and Pd nanoboxes exhibited different behavior, as demonstrated in Figure 27 and Figure 28. The addition of varying amounts of the as synthesized Pd nanoboxes to Ag nanocubes in suspension resulted in a shift in the absorption peak proportional to the amount of Pd nanoboxes added. When repeated with separated Pd nanoboxes and AgPd spheres respectively, the same experiment did not show a similarly large shift in the peak position.

5.4. Conclusions

The synthesis of Ag nanocubes of near-uniform size and high shape selectivity has been demonstrated and subsequently used for the synthesis of Pd nanoboxes. The nanocubes were shown to behave as sacrificial templates for the formation of the Pd nanoboxes as a result of the galvanic displacement effect. The use of $CuCl_2$ to provide the Cl ions used to achieve control of the morphology of the Ag nanoparticles resulted in the formation of some AgCu alloy nanocubes within the sample, as confirmed by the peaks appearing in XRD diffractograms of the pure Ag nanoparticles which do not correspond with the positions of the pure Ag or AgO phases.

The physical mixture of Ag polyhedra and Pd nanoboxes does not show very much activity in UV-Vis, with observed phenomena consisting primarily of damping of the Ag peak and shifting of the baseline absorbance due to the presence of the Pd. The same physical mixtures, with nanocubes substituted for the Ag polyhedra exhibited

evidence of coupling of the observed SPR bands in the form of a shift in the peak position proportional to the amount of Pd nanoboxes added to the suspension. This only occurred with the as-synthesized Pd nanobox suspensions, and not with the fractionated samples, indicating that the presence of both the AgPd spheres and the Pd nanoboxes are necessary to provide the correct conditions for the observed peak shifts to occur.

Chapter 6: Conclusions and Outlook

Morphological control of metal nanoparticles has become a very active area of research in the fields of nanoscience and nanotechnology as a direct consequence of the unique properties such materials possess. Strict and highly selective control of the morphology of nanoparticles is necessary to achieve the synthesis of nanoscale materials with well-defined properties. It is worth noting that, though the crystallization of a nanomaterial into a particular structure is usually kinetically driven, the thermodynamic factors of the system are known to have a large influence on the morphology of the nanomaterial, as many materials exist in a variety of polymorphs based on the environment in which they are synthesized[144]. In addition, the size and morphology of the nanomaterial generated can have profound impacts on its properties, as has been demonstrated in the fields of catalysis and plasmonics, where the surface facets present and the number of sharp corners, respectively, directly determine activity.

Based on the work presented in Chapter 3, we conclude that the size of the Pd nanoparticles synthesized has a direct impact on the rate of conversion of methanol to synthesis gas, as a result of the change in nanoparticle dispersion with nanoparticle diameter. The conversion of methanol increased with increasing surface area-to-bulk ratio, with the trend observed remaining consistent with and without the presence of carbon dioxide in the inlet stream.

Work done on NiPd bimetallic alloy nanocubes (Chapter 4) indicated that control of alloy nanoparticle morphology is possible, and that the nanocubes synthesized are of homogeneous composition and size. Further, it was demonstrated that for most of the synthetic conditions tested, two populations of nanoparticles with differing compositions formed. In short, the synthetic conditions were shown to have a large impact on the morphologies and compositions of the nanoparticles generated, as would be expected based on the kinetic and thermodynamic factors characterizing each synthesis, as described above.

Lastly, in Chapter 5, it was posited that by controlling the shape and composition of Ag and Pd nanoparticles, the wavelengths of their respective SPR peaks could be tuned. Pd nanospheres, which have been shown in the literature to exhibit a low broad absorbance throughout the visible range exhibited the expected absorbance curve in UV-Vis measurements. Ag nanocubes synthesized also behaved as predicted. The Ag polyhedra demonstrated a broad doublet peak most likely a result of the superposition of the peak positions of the populations of nanoparticles present in the suspension. Physical mixtures of Ag polyhedra and the fractionated Pd nanoboxes and AgPd spheres synthesized resulted in a baseline shift and damping of the broad absorbance in the visible range of the spectrum. In contrast, the mixtures of the Ag nanocubes and the synthesized nanoboxes showed a shift in the peak position proportional to the amount of Pd nanobox suspension was added to the physical mixture.

Future directions based on the research presented herein include (i) exploration of scaled up versions of the syntheses described, to make the techniques more commercially viable, (ii) more in-depth characterization of the catalytic properties of bimetallic NiPd

nanocubes as compared to bimetallic nanospheres and (iii) investigation of the response of physical mixtures of Ag nanocubes and Pd nanoboxes when deposited on a substrate rather than suspended in a solvent, for applications in the design of finely tuned and sensitive sensors.

References

1. Kundu, S., K. Wang, S. Lau, and H. Liang, *Photochemical synthesis of shape-selective palladium nanocubes in aqueous solution.* Journal of Nanoparticle Research, 2010: p. 1-13.

2. Ai, F., A. Yao, W. Huang, D. Wang, and X. Zhang, *Synthesis of PVP-protected NiPd nanoalloys by modified polyol process and their magnetic properties.* Physica E, 2010. **42** p. 1281-1286.

3. Hegde, M.S., D. Larcher, L. DuPont, B. Beaudoin, K. Tekaia-Elhsissen, and J.-M. Tarascon, *Synthesis and chemical reactivity of polyol prepared monodisperse nickel powders.* Solid State Ionics, 1997. **93**: p. 33-50.

4. Harris, P.J.F., *Sulphur-induced faceting of platinum catalyst particles.* Nature, 1986. **323**(6091): p. 792-794.

5. Tao, A., P. Sinsermsuksakul, and P. Yang, *Polyhedral Silver Nanocrystals with Distinct Scattering Signatures.* Angewandte Chemie International Edition, 2006. **45**(28): p. 4597-4601.

6. Tao, A.R., S. Habas, and P. Yang, *Shape Control of Colloidal Metal Nanocrystals.* Small, 2008. **4**(3): p. 310-325.

7. Im, S.H., Y.T. Lee, B. Wiley, and Y. Xia, *Large-Scale Synthesis of Silver Nanocubes: The Role of HCl in Promoting Cube Perfection and Monodispersity.* Angewandte Chemie International Edition, 2005. **44**(14): p. 2154-2157.

8. Lee, Y.T., S.H. Im, B. Wiley, and Y. Xia, *Quick formation of single-crystal nanocubes of silver through dual functions of hydrogen gas in polyol synthesis.* Chemical Physics Letters, 2005. **411**(4–6): p. 479-483.

9. Lim, B., M. Jiang, J. Tao, P.H.C. Camargo, Y. Zhu, and Y. Xia, *Shape-Controlled Synthesis of Pd Nanocrystals in Aqueous Solutions.* Advanced Functional Materials, 2009. **19**(2): p. 189-200.

10. Lu, X., M. Rycenga, S.E. Skrabalak, B. Wiley, and Y. Xia, *Chemical Synthesis of Novel Plasmonic Nanoparticles.* Annual Review of Physical Chemistry, 2009. **60**(1): p. 167-192.

11. Rycenga, M., C.M. Cobley, J. Zeng, W. Li, C.H. Moran, Q. Zhang, D. Qin, and Y. Xia, *Controlling the Synthesis and Assembly of Silver Nanostructures for Plasmonic Applications.* Chemical Reviews, 2011. **111**(6): p. 3669-3712.

12. Siekkinen, A.R., J.M. McLellan, J. Chen, and Y. Xia, *Rapid synthesis of small silver nanocubes by mediating polyol reduction with a trace amount of sodium sulfide or sodium hydrosulfide.* Chemical Physics Letters, 2006. **432**(4–6): p. 491-496.

13. Wang, Y., Y. Zheng, C.Z. Huang, and Y. Xia, *Synthesis of Ag Nanocubes 18–32 nm in Edge Length: The Effects of Polyol on Reduction Kinetics, Size Control, and Reproducibility.* Journal of the American Chemical Society, 2013. **135**(5): p. 1941-1951.

14. Wiley, B., Y. Sun, and Y. Xia, *Synthesis of Silver Nanostructures with Controlled Shapes and Properties.* Accounts of Chemical Research, 2007. **40**(10): p. 1067-1076.

15. Zeng, J., Y. Zheng, M. Rycenga, J. Tao, Z.-Y. Li, Q. Zhang, Y. Zhu, and Y. Xia, *Controlling the Shapes of Silver Nanocrystals with Different Capping Agents.* Journal of the American Chemical Society, 2010. **132**(25): p. 8552-8553.

16. Sau, T.K. and A.L. Rogach, *Colloidal Synthesis of Noble Metal Nanoparticles of Complex Morphologies*, in *Complex-Shaped Metal Nanoparticles*. 2012, Wiley-VCH Verlag GmbH & Co. KGaA. p. 7-90.

17. Cui, C.-H. and S.-H. Yu, *Controlling Morphology in Noble Metal Nanoparticles via Templating Approach*, in *Complex-Shaped Metal Nanoparticles*. 2012, Wiley-VCH Verlag GmbH & Co. KGaA. p. 91-116.

18. Sun, Y., B.T. Mayers, and Y. Xia, *Template-Engaged Replacement Reaction: A One-Step Approach to the Large-Scale Synthesis of Metal Nanostructures with Hollow Interiors.* Nano Letters, 2002. **2**(5): p. 481-485.

19. Chen, J., B. Wiley, J. McLellan, Y. Xiong, Z.-Y. Li, and Y. Xia, *Optical Properties of Pd−Ag and Pt−Ag Nanoboxes Synthesized via Galvanic Replacement Reactions.* Nano Letters, 2005. **5**(10): p. 2058-2062.

20. Skrabalak, S.E., J. Chen, Y. Sun, X. Lu, L. Au, C.M. Cobley, and Y. Xia, *Gold Nanocages: Synthesis, Properties, and Applications.* Accounts of Chemical Research, 2008. **41**(12): p. 1587-1595.

21. Tanaka, K.-i. and A. Sasahara, *Reconstructive activation of bimetallic surfaces: Catalytic reduction of NO with H2 on Pt(100), Pt(110), Rh(100), Rh(110) and bimetallic single crystal surfaces of Rh/Pt(100), Rh/Pt(110), Pt/Rh(100), and Pt/Rh(110).* Journal of Molecular Catalysis A: Chemical, 2000. **155**(1–2): p. 13-22.

22. Carberry, J.J., *Structure sensitivity in heterogeneous catalysis: Activity and yield/selectivity.* Journal of Catalysis, 1988. **114**(2): p. 277-283.

23. Miyamoto, A., M. Miura, Y. Murakami, and K. Mori, *Structure Sensitivity in Catalysis of Vanadium Oxide*, in *Studies in Surface Science and Catalysis*, M. Che and G.C. Bond, Editors. 1985, Elsevier. p. 371-380.

24. Germain, J.E., *Structure-Sensitive Catalytic Reactions on Oxide Surfaces*, in *Studies in Surface Science and Catalysis*, M. Che and G.C. Bond, Editors. 1985, Elsevier. p. 355-370.

25. Fischer, N., E. van Steen, and M. Claeys, *Structure sensitivity of the Fischer–Tropsch activity and selectivity on alumina supported cobalt catalysts.* Journal of Catalysis, 2013. **299**(0): p. 67-80.

26. Bordes, E., *Comparative Study of Structure-Sensitive Oxidations of n-Butane and 1-Butene in Maleic Anhydride on Two Kinds of Catalysts*, in *Studies in Surface Science and Catalysis*, G. Centi and F. Trifiro, Editors. 1990, Elsevier. p. 585-593.

27. Cui, Y., H. Xu, Q. Ge, Y. Wang, S. Hou, and W. Li, *Structure sensitive dissociation of CH4 on Ni/α-Al2O3: Ni nano-scale particles linearly compensate the Ea and ln A for the CH4 pulse kinetics.* Journal of Molecular Catalysis A: Chemical, 2006. **249**(1–2): p. 53-59.

28. Tanaka, K.-i. and N. Takehiro, *Atomic-scale mechanism for the activation of catalyst surfaces.* Journal of Molecular Catalysis A: Chemical, 1999. **141**(1–3): p. 39-55.

29. Chowdhury, S., V.R. Bhethanabotla, and R. Sen, *Effect of Ag−Cu Alloy Nanoparticle Composition on Luminescence Enhancement/Quenching.* The Journal of Physical Chemistry C, 2009. **113**(30): p. 13016-13022.

30. Brus, L., *Noble Metal Nanocrystals: Plasmon Electron Transfer Photochemistry and Single-Molecule Raman Spectroscopy.* Accounts of Chemical Research, 2008. **41**(12): p. 1742-1749.

31. Guerrero-Martínez, A., S. Barbosa, I. Pastoriza-Santos, and L.M. Liz-Marzán, *Nanostars shine bright for you: Colloidal synthesis, properties and applications of branched metallic nanoparticles.* Current Opinion in Colloid & Interface Science, 2011. **16**(2): p. 118-127.

32. Si, G., W. Shi, K. Li, and Z. Ma, *Synthesis of PSS-capped triangular silver nanoplates with tunable SPR.* Colloids and Surfaces A: Physicochemical and Engineering Aspects, 2011. **380**(1-3): p. 257-260.

33. Tam, F., G.P. Goodrich, B.R. Johnson, and N.J. Halas, *Plasmonic Enhancement of Molecular Fluorescence.* Nano Letters, 2007. **7**(2): p. 496-501.

34. Crespo-Quesada, M., J.-M. Andanson, A. Yarulin, B. Lim, Y. Xia, and L. Kiwi-Minsker, *UV–Ozone Cleaning of Supported Poly(vinylpyrrolidone)-Stabilized Palladium Nanocubes: Effect of Stabilizer Removal on Morphology and Catalytic Behavior*. Langmuir, 2011. **27**(12): p. 7909-7916.

35. Crespo-Quesada, M., A. Yarulin, M. Jin, Y. Xia, and L. Kiwi-Minsker, *Structure Sensitivity of Alkynol Hydrogenation on Shape- and Size-Controlled Palladium Nanocrystals: Which Sites Are Most Active and Selective?* Journal of the American Chemical Society, 2011. **133**(32): p. 12787-12794.

36. Teranishi, T. and M. Miyake, *Size Control of Palladium Nanoparticles and Their Crystal Structures.* Chemistry of Materials, 1998. **10**(2): p. 594-600.

37. Chen, Y., B. He, T. Huang, and H. Liu, *Controlled synthesis of palladium icosahedra nanocrystals by reducing H2PdCl4 with tetraethylene glycol.* Colloids and Surfaces A: Physicochemical and Engineering Aspects, 2009. **348**(1-3): p. 145-150.

38. McLellan, J.M., Y. Xiong, M. Hu, and Y. Xia, *Surface-enhanced Raman scattering of 4-mercaptopyridine on thin films of nanoscale Pd cubes, boxes, and cages.* Chemical Physics Letters, 2006. **417**(1-3): p. 230-234.

39. Choo, H., B. He, K.Y. Liew, H. Liu, and J. Li, *Morphology and control of Pd nanoparticles.* Journal of Molecular Catalysis A: Chemical, 2006. **244** p. 217–228.

40. Sun, Y. and Y. Xia, *Shape-Controlled Synthesis of Gold and Silver Nanoparticles.* Science, 2002. **298**(5601): p. 2176-2179.

41. Kim, F., S. Connor, H. Song, T. Kuykendall, and P. Yang, *Platonic Gold Nanocrystals.* Angewandte Chemie International Edition, 2004. **43**(28): p. 3673-3677.

42. Andrade Sales, E., B. Benhamida, V. Caizergues, J.-P. Lagier, F. Fiévet, and F. Bozon-Verduraz, *Alumina-supported Pd, Ag and Pd-Ag catalysts: Preparation through the polyol process, characterization and reactivity in hexa-1,5-diene hydrogenation.* Applied Catalysis A: General, 1998. **172**(2): p. 273-283.

43. Song, H., F. Kim, S. Connor, G.A. Somorjai, and P. Yang, *Pt Nanocrystals: Shape Control and Langmuir−Blodgett Monolayer Formation.* The Journal of Physical Chemistry B, 2004. **109**(1): p. 188-193.

44. Tsung, C.-K., J.N. Kuhn, W. Huang, C. Aliaga, L.-I. Hung, G.A. Somorjai, and P. Yang, *Sub-10 nm Platinum Nanocrystals with Size and Shape Control: Catalytic Study for Ethylene and Pyrrole Hydrogenation.* Journal of the American Chemical Society, 2009. **131**(16): p. 5816-5822.

45. Narayanan, R. and M.A. El-Sayed, *Catalysis with Transition Metal Nanoparticles in Colloidal Solution: Nanoparticle Shape Dependence and Stability.* The Journal of Physical Chemistry B, 2005. **109**(26): p. 12663-12676.

46. Li, Y.D., C.W. Li, H.R. Wang, L.Q. Li, and Y.T. Qian, *Preparation of nickel ultrafine powder and crystalline film by chemical control reduction.* Materials Chemistry and Physics, 1999. **59**(1): p. 88-90.

47. Hu, H. and K. Sugawara, *Selective synthesis of metallic nickel particles with control of shape via wet chemical process.* Materials Letters, 2008. **62**(28): p. 4339-4342.

48. Kurihara, L.K., G.M. Chow, and P.E. Schoen, *Nanocrystalline metallic powders and films produced by the polyol method.* Nanostructured Materials, 1995. **5**(6): p. 607-613.

49. Libor, Z. and Q. Zhang, *The synthesis of nickel nanoparticles with controlled morphology and SiO2/Ni core-shell structures.* Materials Chemistry and Physics, 2009. **114**(2-3): p. 902-907.

50. Hu, H. and K. Sugawara, *Ag-catalyzed synthesis of ultrafine nickel nanoparticles: A facile way to size control.* Materials Letters, 2009. **63**(11): p. 940-942.

51. Qiang, L. and D. Weimin, *Large-Scale Synthesis and Catalytic Properties of Nearly Monodispersive Nickel 3D Nanostructures.* Rare Metal Materials and Engineering, 2009. **38**(12): p. 2080-2084.

52. Kim, K.H., Y.B. Lee, E.Y. Choi, H.C. Park, and S.S. Park, *Synthesis of nickel powders from various aqueous media through chemical reduction method.* Materials Chemistry and Physics, 2004. **86**(2-3): p. 420-424.

53. Semagina, N. and L. Kiwi-Minsker, *Recent Advances in the Liquid-Phase Synthesis of Metal Nanostructures with Controlled Shape and Size for Catalysis.* Catalysis Reviews: Science and Engineering, 2009. **51**(2): p. 147 - 217.

54. Telkar, M.M., C.V. Rode, R.V. Chaudhari, S.S. Joshi, and A.M. Nalawade, *Shape-controlled preparation and catalytic activity of metal nanoparticles for hydrogenation of 2-butyne-1,4-diol and styrene oxide.* Applied Catalysis A: General, 2004. **273**(1-2): p. 11-19.

55. Nagaveni, K., A. Gayen, G.N. Subbanna, and M.S. Hegde, *Pd-coated Ni nanoparticles by the polyol method: an efficient hydrogenation catalyst.* Journal of Materials Chemistry, 2002. **12**(10): p. 3147-3151.

56. Lu, P., T. Teranishi, K. Asakura, M. Miyake, and N. Toshima, *Polymer-Protected Ni/Pd Bimetallic Nano-Clusters: Preparation, Characterization and Catalysis for Hydrogenation of Nitrobenzene.* The Journal of Physical Chemistry B, 1999. **103**(44): p. 9673-9682.

57. Montejano-Carrizales, J.M., J.L. Rodríguez-López, U. Pal, M. Miki-Yoshida, and M. José-Yacamán, *The Completion of the Platonic Atomic Polyhedra: The Dodecahedron.* Small, 2006. **2**(3): p. 351-355.

58. Cuya Huaman, J.L., S. Fukao, K. Shinoda, and B. Jeyadevan, *Novel standing Ni-Pt alloy nanocubes.* CrystEngComm, 2011. **13**(10): p. 3364-3369.

59. Carenco, S., C.d. Boissière, L. Nicole, C.m. Sanchez, P. Le Floch, and N. Mézailles, *Controlled Design of Size-Tunable Monodisperse Nickel Nanoparticles.* Chemistry of Materials, 2010. **22**(4): p. 1340-1349.

60. Chen, D., K.O. Christensen, E. Ochoa-Fernandez, Z. Yu, B. Tøtdal, N. Latorre, A. Monzon, and A. Holmen, *Synthesis of Carbon Nanofibers: Effects of Ni Crystal Size during Methane Decomposition.* Journal of Catalysis, 2005. **229** p. 82-96.

61. Christensen, K.O., D. Chen, R. Lødeng, and A. Holmen, *Effect of supports and Ni crystal size on carbon formation and sintering during steam methane reforming.* Applied Catalysis A: General, 2006. **314** p. 9-22.

62. Kamyabi-Gol, A., S.M. Zebarjad, and S.A. Sajjadi, *A study on the effect of synthesis parameters on the size of nickel particles in sol–gel derived Ni–SiO2–Al2O3 nanocomposites.* Journal of Sol-Gel Science and Technology, 2009. **51**(1): p. 92-101.

63. Li, D. and S. Komarneni, *Microwave-Assisted Polyol Process for Synthesis of Ni Nanoparticles.* Journal of the American Ceramic Society, 2006. **89**(5): p. 1510-1517.

64. Metin, O., V. Mazumder, S. Ozkar, and S.S. Sun, *Monodisperse Nickel Nanoparticles; and Their Catalysis in Hydrolytic Dehydrogenation of Ammonia Borane.* Journal of the American Chemical Society, 2010. **132**(5): p. 1468-+.

65. Winnischofer, H., T.C.R. Rocha, W.C. Nunes, L.M. Socolovsky, M. Knobel, and D. Zanchet, *Chemical Synthesis and Structural Characterization of Highly Disordered Ni Colloidal Nanoparticles.* ACS Nano, 2008. **2**(6): p. 1313-1319.

66. Hou, Y., H. Kondoh, T. Ohta, and S. Gao, *Size-controlled synthesis of nickel nanoparticles.* Applied Surface Science, 2005. **241**(1-2): p. 218-222.

67. Chen, M., J. Falkner, W.-H. Guo, J.-Y. Zhang, C. Sayes, and V.L. Colvin, *Synthesis and self-organization of soluble monodisperse palladium nanoclusters.* Journal of Colloid and Interface Science, 2005. **287**(1): p. 146-151.

68. Li, Y., E. Boone, and M.A. El-Sayed, *Size Effects of PVP−Pd Nanoparticles on the Catalytic Suzuki Reactions in Aqueous Solution.* Langmuir, 2002. **18**(12): p. 4921-4925.

69. Deckers, S., F.H.P.M. Habraken, W.F. van der Weg, A.W.D. van der Gon, J.F. van der Veen, and J.W. Geus, *Oxidation-induced segregation at the Pt0.5Ni0.5(111) surface studied by medium-energy ion scattering.* Applied Surface Science, 1990. **45**(2): p. 121-129.

70. Sun, S.-G. and Y.-Y. Yang, *Studies of kinetics of HCOOH oxidation on Pt(100), Pt(110), Pt(111), Pt(510) and Pt(911) single crystal electrodes.* Journal of Electroanalytical Chemistry, 1999. **467**(1-2): p. 121-131.

71. Erikson, H., A. Sarapuu, K. Tammeveski, J. Solla-Gullón, and J.M. Feliu, *Enhanced electrocatalytic activity of cubic Pd nanoparticles towards the oxygen reduction reaction in acid media.* Electrochemistry Communications, 2011. **13**(7): p. 734-737.

72. Kondo, S., M. Nakamura, N. Maki, and N. Hoshi, *Active Sites for the Oxygen Reduction Reaction on the Low and High Index Planes of Palladium.* The Journal of Physical Chemistry C, 2009. **113**(29): p. 12625-12628.

73. Zhou, Y.-H., P.-H. Lv, and G.-C. Wang, *DFT studies of methanol decomposition on Ni(100) surface: Compared with Ni(111) surface.* Journal of Molecular Catalysis A: Chemical, 2006. **258**(1-2): p. 203-215.

74. Derry, G.N., R. Wan, F. Strauch, and C. English, *Segregation and interlayer relaxation at the NiPd(111) surface.* Journal of Vacuum Science & Technology A, 2011. **29**(1).

75. Derry, G.N., C.B. McVey, and P.J. Rous, *The surface structure and segregation profile of Ni50Pd50(100): a dynamical LEED study.* Surface Science, 1995. **326**(1-2): p. 59-66.

76. Derry, G.N. and R. Wan, *Comparison of surface structure and segregation in AgAu and NiPd alloys.* Surface Science, 2004. **566**: p. 862-868.

77. Menning, C.A. and J.G. Chen, *Thermodynamics and kinetics of oxygen-induced segregation of 3d metals in Pt–3d–Pt(111) and Pt–3d–Pt(100) bimetallic structures.* Journal of Chemical Physics, 2008. **128**(16): p. 4703-4712.

78. Bertolini, J.C., P. Miegge, P. Hermann, J.L. Rousset, and B. Tardy, *On the reactivity of 2D Pd surface alloys obtained by surface segregation or deposition technique.* Surface Science, 1995. **331-333, Part A**(0): p. 651-658.

79. Michel, A.C., L. Lianos, J.L. Rousset, P. Delichère, N.S. Prakash, J. Massardier, Y. Jugnet, and J.C. Bertolini, *Surface characterization and reactivity of Pd8Ni92 (111) and (110) alloys.* Surface Science, 1998. **416**(1-2): p. 288-294.

80. Miegge, P., J.L. Rousset, B. Tardy, J. Massardier, and J.C. Bertolini, *PD1NI99 AND PD5NI95 - PD SURFACE SEGREGATION AND REACTIVITY FOR THE HYDROGENATION OF 1,3-BUTADIENE.* Journal of Catalysis, 1994. **149**(2): p. 404-413.

81. Helfensteyn, S., J. Luyten, L. Feyaerts, and C. Creemers, *Modelling surface phenomena in Pd-Ni alloys.* Applied Surface Science, 2003. **212-213**(0): p. 844-849.

82. Løvvik, O.M., *Surface segregation in palladium based alloys from density-functional calculations.* Surface Science, 2005. **583**(1): p. 100-106.

83. Menon, M. and B.C. Khanra, *Spatial distribution of atoms in gas-covered Pd-X nanoparticles (X = Ag, Cu, Ni, Pt).* International Journal of Modern Physics B, 2000. **14**(16): p. 1683-1692.

84. Ma, Y. and P.B. Balbuena, *Surface segregation in bimetallic Pt3M (M=Fe, Co, Ni) alloys with adsorbed oxygen.* Surface Science, 2009. **603**(2): p. 349-353.

85. Menning, C.A. and J.G.G. Chen, *General trend for adsorbate-induced segregation of subsurface metal atoms in bimetallic surfaces.* Journal of Chemical Physics, 2009. **130**(17).

86. McLellan, J.M., A. Siekkinen, J. Chen, and Y. Xia, *Comparison of the surface-enhanced Raman scattering on sharp and truncated silver nanocubes.* Chemical Physics Letters, 2006. **427**(1-3): p. 122-126.

87. Grace, A.N. and K. Pandian, *One pot synthesis of polymer protected Pt, Pd, Ag and Ru nanoparticles and nanoprisms under reflux and microwave mode of heating in glycerol - A comparative study.* Materials Chemistry and Physics, 2007. **104** p. 191-198.

88. El-Ansary, A. and L.M. Faddah, *Nanoparticles as biochemical sensors.* Nanotechnol., Sci. Appl., 2010. **3**(Copyright (C) 2011 American Chemical Society (ACS). All Rights Reserved.): p. 65-76.

89. Shtykov, S.N. and T.Y. Rusanova, *Nanomaterials and nanotechnologies in chemical and biochemical sensors: Capabilities and applications.* Russ. J. Gen. Chem., 2008. **78**(Copyright (C) 2011 American Chemical Society (ACS). All Rights Reserved.): p. 2521-2531.

90. Hu, J., M. Jiang, and Z. Lin, *Novel technology for depositing a Pd-Ag alloy film on a tapered optical fibre for hydrogen sensing.* J. Opt. A: Pure Appl. Opt., 2005. **7**(Copyright (C) 2011 American Chemical Society (ACS). All Rights Reserved.): p. 593-598.

91. Ohara, S., Y. Hatakeyama, M. Umetsu, K. Sato, T. Naka, and T. Adschiri, *Palladium–polyelectrolyte hybrid nanoparticles for hydrogen sensor in fuel cells.* Journal of Power Sources, 2009. **193** p. 367-370.

92. Wang, M. and Y. Feng, *Palladium-silver thin film for hydrogen sensing.* Sens. Actuators, B, 2007. **B123**(Copyright (C) 2011 American Chemical Society (ACS). All Rights Reserved.): p. 101-106.

93. Cuenya, B.R., *Synthesis and catalytic properties of metal nanoparticles: Size, shape, support, composition, and oxidation state effects.* Thin Solid Films, 2010. **518**(12): p. 3127-3150.

94. Chen, E., H. Su, W. Zhang, and T. Tan, *A novel shape-controlled synthesis of dispersed silver nanoparticles by combined bioaffinity adsorption and TiO2 photocatalysis.* Powder Technology, 2011. **212**(1): p. 166-172.

95. Lee, C.-L., C.-M. Tseng, R.-B. Wu, C.-C. Wu, and S.-C. Syu, *Catalytic characterization of hollow silver/palladium nanoparticles synthesized by a displacement reaction.* Electrochimica Acta, 2009. **54**(23): p. 5544-5547.

96. Mitsuishi, M., H. Tanaka, M. Obata, and T. Miyashita, *Plasmon-Enhanced Luminescence from Ultrathin Hybrid Polymer Nanoassemblies for Microscopic Oxygen Sensor Application.* Langmuir, 2010. **26**(Copyright (C) 2011 American Chemical Society (ACS). All Rights Reserved.): p. 15117-15120.

97. Humbert, M.P., L.E. Murillo, and J.G. Chen, *Rational Design of Platinum-Based Bimetallic Catalysts with Enhanced Hydrogenation Activity.* ChemPhysChem, 2008. **9**(9): p. 1262-1264.

98. Khan, N., L. Murillo, Y. Shu, and J. Chen, *Correlating Low-temperature Hydrogenation Activity of Co/Pt(111) Bimetallic Surfaces to Supported Co/Pt/γ-Al_2O_3 Catalysts.* Catalysis Letters, 2005. **105**(3): p. 233-238.

99. Kitchin, J.R., N.A. Khan, M.A. Barteau, J.G. Chen, B. Yakshinskiy, and T.E. Madey, *Elucidation of the active surface and origin of the weak metal–hydrogen bond on Ni/Pt(1 1 1) bimetallic surfaces: a surface science and density functional theory study.* Surface Science, 2003. **544**(2-3): p. 295-308.

100. Murillo, L.E. and J.G. Chen, *Adsorption and reaction of propanal, 2-propenol and 1-propanol on Ni/Pt(111) bimetallic surfaces.* Surface Science, 2008. **602** p. 2412-2420.

101. Corcoran, C.J., H. Tavassol, M.A. Rigsby, P.S. Bagus, and A. Wieckowski, *Application of XPS to study electrocatalysts for fuel cells.* Journal of Power Sources, 2010. **195**(24): p. 7856-7879.

102. Borchert, H., B. Jürgens, T. Nowitzki, P.Behrend, Y. Borchert, V. Zielasek, S. Giorgio, C.R. Henry, and M. Bäumer, *Decomposition of methanol by Pd, Co, and bimetallic Co–Pd catalysts: A combined study of well-defined systems under ambient and UHV conditions.* Journal of Catalysis, 2008. **256**: p. 24–36.

103. Singh, S.K., Y. Iizuka, and Q. Xu, *Nickel-palladium nanoparticle catalyzed hydrogen generation from hydrous hydrazine for chemical hydrogen storage.* International Journal of Hydrogen Energy, 2011. **36**(18): p. 11794-11801.

104. Coq, B. and F. Figueras, *Bimetallic palladium catalysts: influence of the co-metal on the catalyst performance.* Journal of Molecular Catalysis A: Chemical, 2001. **173**(1-2): p. 117-134.

105. Kittel, C., *Introduction to Solid State Physics*. 4th ed. 1971: John Wiley and Sons.

106. *XAFS, EXAFS, and XANES*. July 7, 2012 November 12, 2012]; Available from: http://www.xafs.org/.

107. Hokenek, S. and J.N. Kuhn, *Methanol Decomposition over Palladium Particles Supported on Silica: Role of Particle Size and Co-Feeding Carbon Dioxide on the Catalytic Properties.* ACS Catalysis, 2012. **2**(6): p. 1013-1019.

108. Ravel, B. and M. Newville, *ATHENA, ARTEMIS, HEPHAESTUS: Data Analysis for X-ray Absorption Spectroscopy Using IFEFFIT.* Journal of Synchrotron Radiation, 2005. **12**: p. 537-541.

109. Newville, M., *IFEFFIT: Interactive XAFS Analysis and FEFF Fitting.* Journal of Synchrotron Radiation, 2001. **8**: p. 322– 324.

110. Chen, J.G., *NEXAFS investigations of transition metal oxides, nitrides, carbides, sulfides and other interstitial compounds.* Surface Science Reports, 1997. **30**(1–3): p. 1-152.

111. Aslan, K., J. Lakowicz, and C. Geddes, *Metal-enhanced fluorescence using anisotropic silver nanostructures: critical progress to date.* Analytical and Bioanalytical Chemistry, 2005. **382**(4): p. 926-933.

112. Lakowicz, J.R., *Radiative Decay Engineering: Biophysical and Biomedical Applications.* Analytical Biochemistry, 2001. **298**(1): p. 1-24.

113. Lakowicz, J.R., J. Malicka, I. Gryczynski, Z. Gryczynski, and C.D. Geddes, *Radiative Decay Engineering: The Role of Photonic Mode Density in Biotechnology.* Journal of Physics D: Applied Physics, 2003. **36**: p. R240-R249.

114. Lakowicz, J.R., Y. Shen, S. D'Auria, J. Malicka, J. Fang, Z. Gryczynski, and I. Gryczynski, *Radiative Decay Engineering: 2. Effects of Silver Island Films on Fluorescence Intensity, Lifetimes, and Resonance Energy Transfer.* Analytical Biochemistry, 2002. **301**(2): p. 261-277.

115. Malicka, J., I. Gryczynski, Z. Gryczynski, and J.R. Lakowicz, *Effects of fluorophore-to-silver distance on the emission of cyanine–dye-labeled oligonucleotides.* Analytical Biochemistry, 2003. **315**(1): p. 57-66.

116. Zhang, J., E. Matveeva, I. Gryczynski, Z. Leonenko, and J.R. Lakowicz, *Metal-Enhanced Fluoroimmunoassay on a Silver Film by Vapor Deposition.* The Journal of Physical Chemistry B, 2005. **109**(16): p. 7969-7975.

117. Aslan, K., S.N. Malyn, and C.D. Geddes, *Metal-Enhanced Fluorescence from Large Gold Colloids on Planar Surfaces: Angular Dependent Emission.* Journal of Fluorescence, 2007. **17**(1): p. 7-13.

118. Dulkeith, E., M. Ringler, T.A. Klar, J. Feldmann, A. Muñoz Javier, and W.J. Parak, *Gold Nanoparticles Quench Fluorescence by Phase Induced Radiative Rate Suppression.* Nano Letters, 2005. **5**(4): p. 585-589.

119. Pompa, P.P., MartiradonnaL, A.D. Torre, F.D. Sala, MannaL, M. De Vittorio, CalabiF, CingolaniR, and RinaldiR, *Metal-enhanced fluorescence of colloidal nanocrystals with nanoscale control.* Nat Nano, 2006. **1**(2): p. 126-130.

120. Zhang, Y., K. Aslan, M.J.R. Previte, and C.D. Geddes, *Metal-Enhanced Fluorescence from Copper Substrates.* Applied Physics Letters, 2007. **90**: p. 173116.

121. Cazayous, M., C. Langlois, T. Oikawa, C. Ricolleau, and A. Sacuto, *Cu-Ag core-shell nanoparticles: A direct correlation between micro-Raman and electron microscopy.* Physical Review B, 2006. **73**(11): p. 113402.

122. Nakamura, T., Y. Tsukahara, T. Yamauchi, T. Sakata, H. Mori, and Y. Wada, *Preparation of Ag Core-Cu Shell Nanoparticles by Microwave-assisted Alcohol Reduction Process.* Chemistry Letters, 2007. **36**(1): p. 154-155.

123. Tsuji, M., S. Hikino, R. Tanabe, and D. Yamaguchi, *Synthesis of Ag@Cu Core-Shell Nanoparticles in High Yield Using a Polyol Method.* Chemistry Letters, 2010. **39**(4): p. 334-336.

124. Carlsson, A.F., M. Naschitzki, M. Bäumer, and H.J. Freund, *Adsorption and reaction on pristine and oxidized Co-Pd bimetallic particles supported on Al2O3 thin films.* Surface Science, 2003. **545**(1-2): p. 143-153.

125. Conant, T., A. M.Karima, V. Lebarbier, Y. Wang, F. Girgsdies, R. Schlögl, and A. Datye, *Stability of bimetallic Pd–Zn catalysts for the steam reforming of methanol.* Journal of Catalysis 2008. **257**: p. 64–70.

126. Elhamdaoui, A., G. Bergeret, J. Massardier, M. Primet, and A. Renouprez, *CO and NO Interaction with Pd-Ag and Pd-Cr Bimetallic Catalysts .: 1. X-Ray-Diffraction, Infrared-Spectroscopy, and Thermoreaction.* Journal of Catalysis, 1994. **148**(1): p. 47-55.

127. Fıçıcılar, B., A. Bayrakçeken, and İ. Eroğlu, *Effect of Pd loading in Pd-Pt bimetallic catalysts doped into hollow core mesoporous shell carbon on performance of proton exchange membrane fuel cells.* Journal of Power Sources, 2009. **193**(1): p. 17-23.

128. Hungría, A.B., J.J. Calvino, J.A. Anderson, and A. Martínez-Arias, *Model bimetallic Pd-Ni automotive exhaust catalysts: Influence of thermal aging and hydrocarbon self-poisoning.* Applied Catalysis B: Environmental, 2006. **62** p. 359–368.

129. Jiang, Q., L. Jiang, H. Hou, J. Qi, S. Wang, and G. Sun, *Promoting Effect of Ni in PtNi Bimetallic Electrocatalysts for the Methanol Oxidation Reaction in Alkaline Media: Experimental and Density Functional Theory Studies.* The Journal of Physical Chemistry C, 2010. **114**(46): p. 19714-19722.

130. Khan, N.A., A. Uhl, S. Shaikhutdinov, and H.J. Freund, *Alumina supported model Pd-Ag catalysts: A combined STM, XPS, TPD and IRAS study.* Surface Science, 2006. **600**(9): p. 1849-1853.

131. Lee, A.F., C.V. Ellis, K. Wilson, and N.S. Hondow, *In situ studies of titania-supported Au shell-Pd core nanoparticles for the selective aerobic oxidation of crotyl alcohol.* Catalysis Today, 2010. **In Press, Corrected Proof**.

132. Lonergan, W.W., D.G. Vlachos, and J.G. Chen, *Correlating extent of Pt–Ni bond formation with low-temperature hydrogenation of benzene and 1,3-butadiene over supported Pt/Ni bimetallic catalysts.* Journal of Catalysis, 2010. **271** p. 239-250.

133. Mukainakano, Y., K. Yoshida, S. Kado, K. Okumura, K. Kunimori, and K. Tomishige, *Catalytic performance and characterization of Pt–Ni bimetallic catalysts for oxidative steam reforming of methane.* Chemical Engineering Science, 2008. **63** p. 4891 - 4901.

134. P. Hermann, J.M. Guigner, B. Tardy, Y. Jugnet, D. Simon, and J.-C. Bertolini, *The Pd/Ni(110) Bimetallic System: Surface Characterisation by LEED, AES, XPS, and LEIS Techniques; New Insight on Catalytic Properties.* Journal of Catalysis, 1996. **163**: p. 169-175.

135. Persson, K., A. Ersson, K. Jansson, N. Iverlund, and S. Järås, *Influence of co-metals on bimetallic palladium catalysts for methane combustion.* Journal of Catalysis, 2005. **231**(1): p. 139-150.

136. Qiu, C., R. Shang, Y. Xie, Y. Bu, C. Li, and H. Ma, *Electrocatalytic activity of bimetallic Pd–Ni thin films towards the oxidation of methanol and ethanol.* Materials Chemistry and Physics, 2010. **120** p. 323-330.

137. Steinhauer, B., M.R. Kasireddy, J. Radnik, and A. Martin, *Development of Ni-Pd bimetallic catalysts for the utilization of carbon dioxide and methane by dry reforming.* Applied Catalysis A: General, 2009. **366** p. 333–341.

138. Telkar, M.M., J.M. Nadgeri, C.V. Rode, and R.V. Chaudhari, *Role of a co-metal in bimetallic Ni–Pt catalyst for hydrogenation of m-dinitrobenzene to m-phenylenediamine.* Applied Catalysis A: General, 2005. **295** p. 23-30.

139. Tzitzios, V.K. and V. Georgakilas, *Catalytic reduction of N2O over Ag-Pd/Al2O3 bimetallic catalysts.* Chemosphere, 2005. **59**(6): p. 887-891.

140. Xiong, D.a., Z. Li, Y. An, R. Ma, and L. Shi, *Novel Au-Pd bimetallic core-shell nanocomplex and its catalytic activity modulation.* Journal of Colloid and Interface Science, 2010. **350**(1): p. 260-267.

141. Yoshimura, Y., M. Toba, T. Matsui, M. Harada, Y. Ichihashi, K.K. Bando, H. Yasuda, H. Ishihara, Y. Morita, and T. Kameoka, *Active phases and sulfur tolerance of bimetallic Pd–Pt catalysts used for hydrotreatment.* Applied Catalysis A: General, 2007. **322** p. 152–171.

142. Dubertret, B., M. Calame, and A.J. Libchaber, *Single-mismatch detection using gold-quenched fluorescent oligonucleotides.* Nat Biotech, 2001. **19**(4): p. 365-370.

143. *Single-mismatch detection using gold-quenched fluorescent oligonucleotides.* Nat Biotech, 2001. **19**(7): p. 680-681.

144. *Metal Nanoparticles of Complex Morphologies: A General Introduction*, in *Complex-Shaped Metal Nanoparticles*. 2012, Wiley-VCH Verlag GmbH & Co. KGaA. p. 1-5.

Appendices

Appendix 1: EXAFS Experimental Details

EXAFS was done as per the supporting information for reference [107]. For data acquisition silica-supported Pd catalyst powders (a mass ~ 50 mg) were ground with a mortar and pestle and pressed into 13 mm diameter pellets using a Carver press operated at 12,500 psi for 30 s. Pressed catalyst pellet thicknesses were adjusted to obtain a linear absorption coefficient near 1.

XAS spectra were collected in transmission mode at the Pd K absorption edge (24350 eV) under ambient conditions, with the scan set to take data from 150 eV before to 30 eV before the edge in 10 eV steps and then to 975 eV after the edge in 2 eV steps (pre-edge/edge region). Three scans were taken per sample to improve the signal-to-noise ratio. Data processing (merging of individual scans and data reduction) was performed with the Athena software package[108, 109].

More information can be found at http://pubs.acs.org/doi/suppl/10.1021/cs200689k/suppl_file/cs200689k_si_001.pdf

Appendix 2: Casino Monte Carlo Simulations

Given an Ag nanoparticle of average side length 56 nm, we simulated acceleration voltages of 25, 10, and 5 kV to determine the approximate range of acceleration voltages to use.

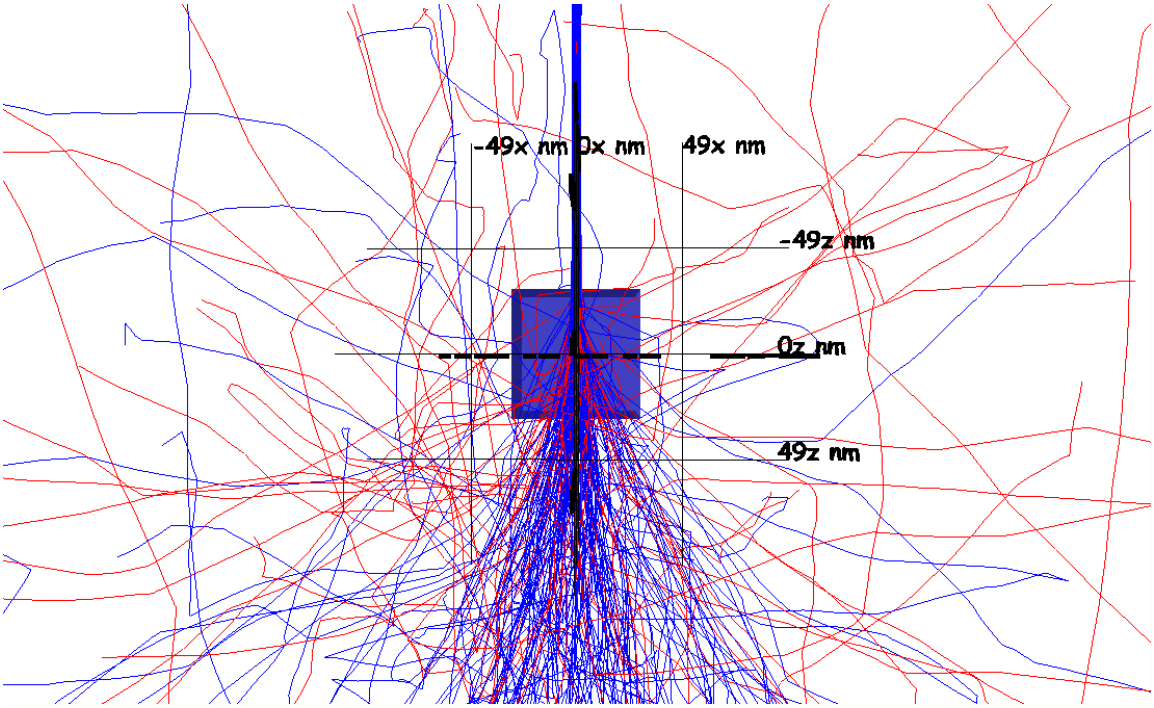

Figure A2-1: Simulated Ag nanocube under a 25 kV electron beam with 5 nm diameter.

As illustrated in Figure A2-1, at 25 kV acceleration voltage, the beam passes right through the sample. This is undesirable since the Ag nanocubes are supported on a Cu formvar TEM grid for analysis. As a result of the high acceleration voltage, the majority of the excitation volume is below the Ag nanocube, and thus most of the signal seen by the EDS detector would be a result of the STEM holder used to image the Cu formvar

Appendix 2 (Continued)

grid. At an acceleration voltage of 10 kV, the same problem is observed as at 25 kV. The results of the Monte Carlo simulation are shown in Figure A2-2.

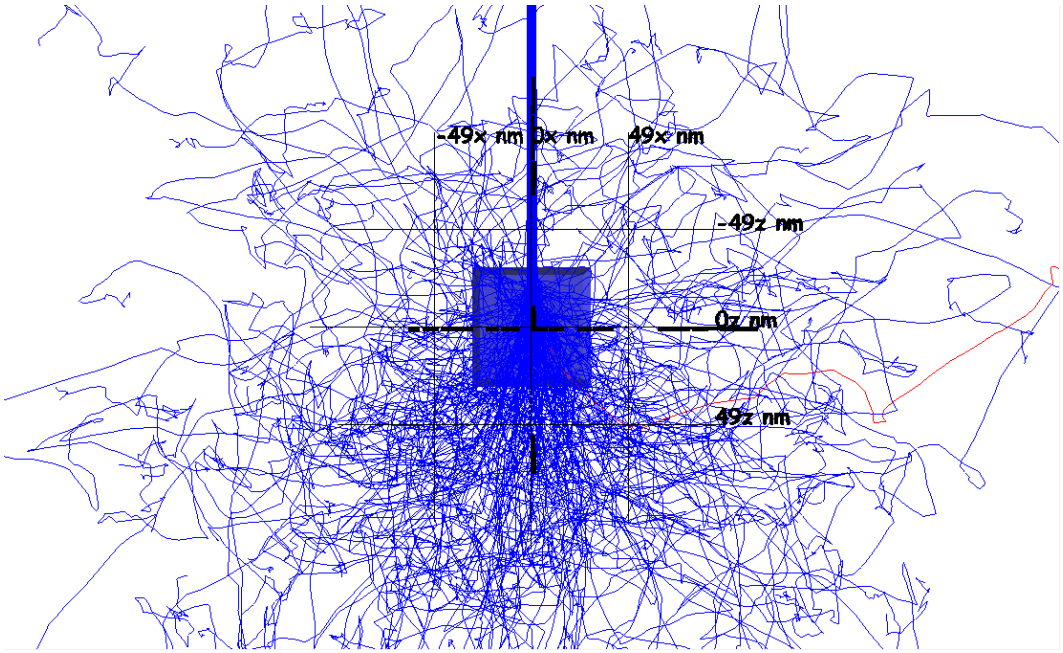

Figure A2-2: Simulated Ag nanocube under a 10 kV electron beam with 5 nm diameter.

At an acceleration voltage of 5 kV, the majority of the excitation volume is contained within the Ag nanocube. However, in order to achieve good counting statistics, a consideration especially important in the case of a sample with a small volume, an acceleration voltage of twice the peak energy is needed. As such, because the Ag Lα peak has an energy of 2.985 eV, an acceleration voltage of 6 kV was used in imaging and EDS measurements.

Appendix 2 (Continued)

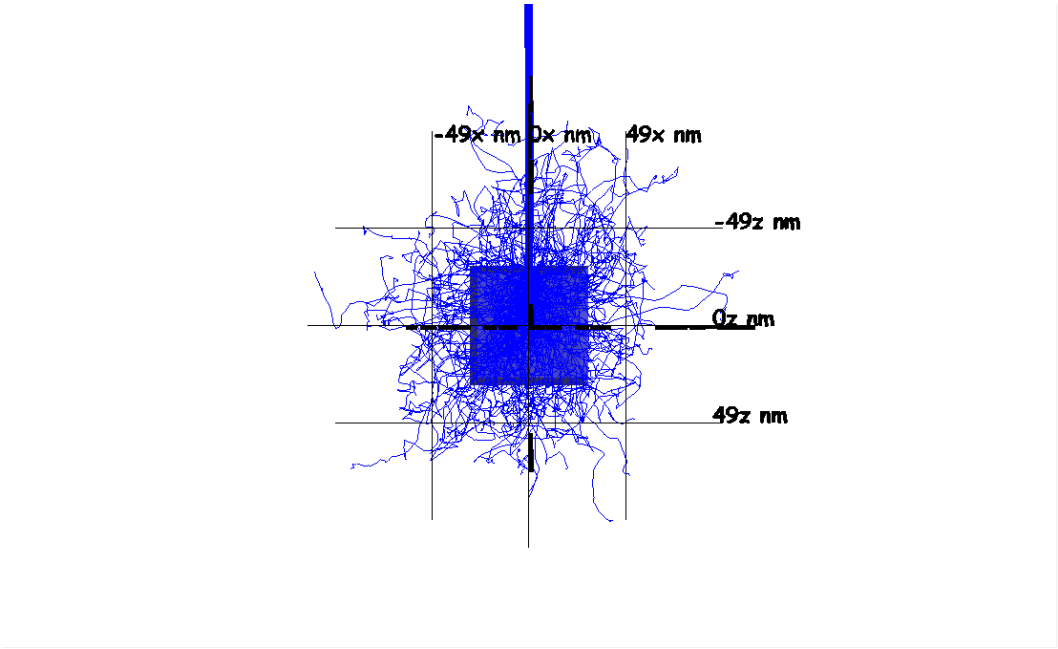

Figure A2-3: Simulated Ag nanocube under a 5 kV electron beam with 5 nm diameter.

Appendix 3: Journal Reprint Permissions

Copyright Clearance Center RightsLink®

Home | Account Info | Help

ACS Publications High quality. High impact.

Title: Methanol Decomposition over Palladium Particles Supported on Silica: Role of Particle Size and Co-Feeding Carbon Dioxide on the Catalytic Properties

Author: Selma Hokenek and John N. Kuhn

Publication: ACS Catalysis

Publisher: American Chemical Society

Date: Jun 1, 2012

Copyright © 2012, American Chemical Society

Logged in as: Selma Hokenek

LOGOUT

Quick Price Estimate

Permission for this particular request is granted for print and electronic formats, and translations, at no charge. Figures and tables may be modified. Appropriate credit should be given. Please print this page for your records and provide a copy to your publisher. Requests for up to 4 figures require only this record. Five or more figures will generate a printout of additional terms and conditions. Appropriate credit should read: "Reprinted with permission from {COMPLETE REFERENCE CITATION}. Copyright {YEAR} American Chemical Society." Insert appropriate information in place of the capitalized words.

◆ Will you be translating is a required field. Please make a selection.

I would like to...	reuse in a Thesis/Dissertation
Requestor Type	Author (original work)
Portion	Full article
Format	Print
Will you be translating?	make a selection
Select your currency	USD - $
Quick Price	Click Quick Price

This service provides permission for reuse only. If you do not have a copy of the article you are using, you may copy and paste the content and reuse according to the terms of your agreement. Please be advised that obtaining the content you license is a separate transaction not involving Rightslink.

QUICK PRICE CONTINUE

To request permission for a type of use not listed, please contact the publisher directly.

Appendix 3 (Continued)

Copyright Clearance Center RightsLink®

Home | Account Info | Help

ACS Publications High quality. High impact.

Title: Controlling the Shapes of Silver Nanocrystals with Different Capping Agents

Author: Jie Zeng, Yiqun Zheng, Matthew Rycenga, Jing Tao, Zhi-Yuan Li, Qiang Zhang, Yimei Zhu, and Younan Xia

Publication: Journal of the American Chemical Society

Publisher: American Chemical Society

Date: Jun 1, 2010

Copyright © 2010, American Chemical Society

Logged in as: Selma Hokenek
Account #: 3000572369
LOGOUT

PERMISSION/LICENSE IS GRANTED FOR YOUR ORDER AT NO CHARGE

This type of permission/license, instead of the standard Terms & Conditions, is sent to you because no fee is being charged for your order. Please note the following:

- Permission is granted for your request in both print and electronic formats, and translations.
- If figures and/or tables were requested, they may be adapted or used in part.
- Please print this page for your records and send a copy of it to your publisher/graduate school.
- Appropriate credit for the requested material should be given as follows: "Reprinted (adapted) with permission from (COMPLETE REFERENCE CITATION). Copyright (YEAR) American Chemical Society." Insert appropriate information in place of the capitalized words.
- One-time permission is granted only for the use specified in your request. No additional uses are granted (such as derivative works or other editions). For any other uses, please submit a new request.

If credit is given to another source for the material you requested, permission must be obtained from that source.

BACK | CLOSE WINDOW

Appendix 3 (Continued)

Copyright Clearance Center RightsLink®

Home | Account Info | Help

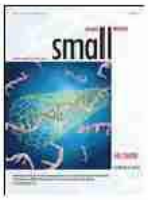

Title: Shape Control of Colloidal Metal Nanocrystals
Author: Andrea R. Tao,Susan Habas,Peidong Yang
Publication: Small
Publisher: John Wiley and Sons
Date: Feb 26, 2008

Logged in as:
Selma Hokenek
Account #: 3000572369
LOGOUT

Order Completed

Thank you very much for your order.

This is a License Agreement between Selma Hokenek ("You") and John Wiley and Sons ("John Wiley and Sons"). The license consists of your order details, the terms and conditions provided by John Wiley and Sons, and the payment terms and conditions.

Get the printable license.

License Number	3090260157285
License date	Feb 15, 2013
Licensed content publisher	John Wiley and Sons
Licensed content publication	Small
Licensed content title	Shape Control of Colloidal Metal Nanocrystals
Licensed copyright line	Copyright © 2008 WILEY-VCH Verlag GmbH & Co. KGaA, Weinheim
Licensed content author	Andrea R. Tao,Susan Habas,Peidong Yang
Licensed content date	Feb 26, 2008
Start page	310
End page	325
Type of use	Dissertation/Thesis
Requestor type	University/Academic
Format	Print and electronic
Portion	Figure/table
Number of figures/tables	1
Original Wiley figure/table number(s)	Figure 4
Will you be translating?	No
Total	0.00 USD

ORDER MORE... CLOSE WINDOW

About the Author

Selma Hokenek is currently a graduate student in the Heterogeneous Catalysis and Materials Chemistry Group at the University of South Florida. She entered USF in 2007 after receiving her B.S.E in Biomedical Engineering at Tulane University, completing an M.S degree in Engineering Sciences in 2009 prior to joining her current research group. Her research interests have focused primarily on morphological and size control of nanoscale materials for applications in catalysis and sensing.